

A simple model to interpret the ultraviolet, optical and infrared emission from galaxies

Elisabete da Cunha^{1*}, Stéphane Charlot¹ and David Elbaz²

¹*Institut d'Astrophysique de Paris, CNRS, Université Pierre & Marie Curie, 98 bis Boulevard Arago, 75014 Paris, France*

²*Laboratoire AIM, CEA/DSM-CNRS-Université Paris Diderot, DAPNIA/Service d'Astrophysique, CEA Saclay, Orme des Merisiers, 91191 Gif-sur-Yvette Cedex, France*

Accepted 2008 June 04. Received 2008 May 30; in original form 2007 December 18

ABSTRACT

We present a simple, largely empirical but physically motivated model to interpret the mid- and far-infrared spectral energy distributions of galaxies consistently with the emission at ultraviolet, optical and near-infrared wavelengths. Our model relies on an existing angle-averaged prescription to compute the absorption of starlight by dust in stellar birth clouds and in the ambient interstellar medium (ISM) in galaxies. We compute the spectral energy distribution of the power reradiated by dust in stellar birth clouds as the sum of three components: a component of polycyclic aromatic hydrocarbons (PAHs); a mid-infrared continuum characterising the emission from hot grains at temperatures in the range 130–250 K; and a component of grains in thermal equilibrium with adjustable temperature in the range 30–60 K. In the ambient ISM, we fix for simplicity the relative proportions of these three components to reproduce the spectral shape of diffuse cirrus emission in the Milky Way, and we include a component of cold grains in thermal equilibrium with adjustable temperature in the range 15–25 K. Our model is both simple and versatile enough that it can be used to derive statistical constraints on the star formation histories and dust contents of large samples of galaxies using a wide range of ultraviolet, optical and infrared observations. We illustrate this by deriving median-likelihood estimates of the star formation rates, stellar masses, effective dust optical depths, dust masses, and relative strengths of different dust components of 66 well-studied nearby star-forming galaxies from the Spitzer Infrared Nearby Galaxy Survey (SINGS). We explore how the constraints derived in this way depend on the available spectral information. From our analysis of the SINGS sample, we conclude that the mid- and far-infrared colours of galaxies correlate strongly with the specific star formation rate, as well as with other galaxy-wide quantities connected to this parameter, such as the ratio of infrared luminosity between stellar birth clouds and the ambient ISM, the contributions by PAHs and grains in thermal equilibrium to the total infrared emission, and the ratio of dust mass to stellar mass. Our model can be straightforwardly applied to interpret ultraviolet, optical and infrared spectral energy distributions from any galaxy sample.

Key words: dust, extinction – galaxies: ISM, stellar content – infrared: galaxies.

1 INTRODUCTION

The spectral energy distributions of galaxies contain valuable information about their contents in stars, gas and dust. Direct ultraviolet, optical and near-infrared radiation from stars provides clues on the past star formation history, chemical enrichment and attenuation by dust. Nebular emission lines produced by the gas heated by young

stars provide further clues on the current star formation activity and the physical conditions of the star-forming gas. At wavelengths $\lambda \gtrsim 3 \mu\text{m}$, the mid- and far-infrared emission reflects the heating of dust in different components of the interstellar medium (ISM) by stars of all ages. Observations at ultraviolet, optical and infrared wavelengths are now becoming available for large samples of galaxies. These include data collected in the ultraviolet by the *Galaxy Evolution Explorer* (GALEX, Martin et al. 2005), in the optical by the Two-degree Field Galaxy Redshift Sur-

* E-mail: dacunha@iap.fr

vey (Colless et al. 2001) and the Sloan Digital Sky Survey (SDSS, Stoughton et al. 2002), in the near-infrared by the Two Micron All Sky Survey (2MASS, Skrutskie et al. 1997), in the mid- and far-infrared by the *Infrared Astronomical Satellite* (IRAS, Beichman et al. 1988), the *Infrared Space Observatory* (ISO, Kessler et al. 1996) and the *Spitzer Space Telescope* (Werner et al. 2004), and in the sub-millimetre by the Sub-millimeter Common User Bolometer Array (SCUBA) on the James Clerk Maxwell Telescope (Holland et al. 1999). Extracting constraints on the stellar populations and ISM of galaxies from these multi-wavelength observations requires the consistent modelling of the emission by stars, gas and dust.

A standard approach to model consistently the emission from stars and dust in galaxies has been to solve the radiative transfer equation for idealised (bulge + disc) spatial distributions of stars and dust (e.g. Rowan-Robinson 1980; Efsthathiou & Rowan-Robinson 1990; Gordon et al. 2001; Misselt et al. 2001; Popescu et al. 2000; Misiriotis et al. 2001). Early models of this type did not include the evolution of stellar populations. Silva et al. (1998) were the first to couple radiative transfer through a dusty ISM and the spectral (and even chemical) evolution of stellar populations. Their model also accounts for the fact that stars are born in dense molecular clouds, which dissipate after some time, and hence, that newly born stars are more attenuated than older stars (see also, e.g., Charlot & Fall 2000; Tuffs et al. 2004). This type of sophisticated model is useful to interpret in detail the emission from individual galaxies in terms of constraints on stellar populations and the spatial distribution and physical properties of the dust. However, because of the complexity of radiative transfer computations, it is not optimised to derive statistical constraints from observations of large samples of galaxies.

A more recent model of starburst galaxies by Dopita et al. (2005, see also Groves et al. 2007) incorporates the consistent treatment of the spectral evolution of stellar populations, the dynamic expansion of H II regions and radiative transfer of starlight through gas and dust. The authors of this model provide a simple parameterization of the ultraviolet, optical and infrared spectra of starburst galaxies by adding the spectra of different types of compact H II regions and their surrounding photo-dissociation regions. This model provides a fast and flexible tool to interpret starburst galaxy spectra in terms of the physical parameters of star-forming regions. However, it is not designed to be applicable to more quiescent galaxies, in which older stellar populations dominate the emission.

In parallel to these theoretical studies, observations by IRAS and ISO have motivated the development of simple, empirically calibrated spectral libraries to interpret the infrared emission from galaxies at wavelengths between 3 and 1000 μm . For example, Chary & Elbaz (2001) and Dale & Helou (2002) both present single-parameter families of infrared spectra to relate an observed spectral energy distribution to either the total infrared luminosity of a galaxy or the intensity of the interstellar radiation field heating the dust. These libraries can be applied easily to the interpretation of large galaxy samples. They have proved useful to characterise the infrared emission from observed galaxies and to investigate the origin of the cosmic infrared background (e.g. Franceschini et al. 2001;

Chary & Elbaz 2001; Elbaz et al. 2002; Lagache et al. 2003, 2004; Dale et al. 2005; Marcillac et al. 2006). A disadvantage of this approach is that it does not relate consistently the infrared emission of the dust to the emission from stellar populations. Another potential limitation is that most existing spectral libraries were calibrated using local galaxy samples, and hence, they may not be applicable to studies of the infrared emission from galaxies at all redshifts (e.g. Pope et al. 2006; Zheng et al. 2007).

In this paper, we present a simple, largely empirical but physically motivated model to interpret the mid- and far-infrared spectral energy distributions of galaxies consistently with the emission at ultraviolet, optical and near-infrared wavelengths. We compute the spectral evolution of stellar populations using the Bruzual & Charlot (2003) population synthesis code. To describe the attenuation of starlight by dust, we appeal to the two-component model of Charlot & Fall (2000). This has been shown to account for the observed relations between the ultraviolet and optical (line and continuum) spectra and the *total* infrared luminosities of galaxies in wide ranges of star-formation activity and dust content (Brinchmann et al. 2004; Kong et al. 2004). We use this model to compute the luminosity absorbed and re-emitted by dust in stellar birth clouds (i.e. giant molecular clouds) and in the ambient (i.e. diffuse) ISM in galaxies. We then distribute this luminosity in wavelength to compute infrared *spectral energy distributions*. We describe the infrared emission from stellar birth clouds as the sum of three components: a component of polycyclic aromatic hydrocarbons (PAHs); a mid-infrared continuum characterising the emission from hot grains at temperatures in the range 130–250 K; and a component of grains in thermal equilibrium with adjustable temperature in the range 30–60 K. In the ambient ISM, we fix for simplicity the relative proportions of these three components to reproduce the spectral shape of diffuse cirrus emission in the Milky Way, and we include a component of cold grains in thermal equilibrium with adjustable temperature in the range 15–25 K.

This simple but versatile model allows us to derive statistical estimates of physical parameters such as star formation rate, stellar mass, dust content and dust properties, from combined ultraviolet, optical and infrared galaxy spectra. To achieve this, we adopt a Bayesian approach similar to that successfully employed by, e.g., Kauffmann et al. (2003), Brinchmann et al. (2004), Gallazzi et al. (2005) and Salim et al. (2007) to interpret ultraviolet, optical and near-infrared galaxy spectra using only the Bruzual & Charlot (2003) and Charlot & Fall (2000) models. As an example, we derive median-likelihood estimates of a set of physical parameters describing the stellar and dust contents of 66 star-forming galaxies from the Spitzer Infrared Nearby Galaxy Survey (SINGS, Kennicutt et al. 2003). Our model reproduces well the observed spectral energy distributions of these galaxies across the entire wavelength range from the far-ultraviolet to the far-infrared, and the star formation histories and dust contents of the galaxies are well constrained. We explore how the constraints derived in this way depend on the available spectral information. From our analysis of the SINGS sample, we conclude that the mid- and far-infrared colours of galaxies are tightly related to the specific star formation rate and to other galaxy-wide properties connected to this parameter.

We present our model of the combined ultraviolet, optical and infrared spectral energy distributions of galaxies in Section 2. In Section 3, we first describe our approach to derive statistical constraints on galaxy physical parameters from multi-wavelength observations. Then, we use this approach to interpret observations of the SINGS galaxy sample taken with *GALEX*, 2MASS, *Spitzer*, *ISO*, *IRAS* and SCUBA. We compare our results to those that would be obtained using previous prescriptions of the infrared emission from galaxies. We also discuss potential sources of systematic errors. Section 4 summarises our conclusions.

2 THE MODEL

In this section, we describe our model to compute the mid- and far-infrared spectral energy distributions of galaxies consistently with the emission at ultraviolet, optical and near-infrared wavelengths. In Section 2.1, we first briefly review the stellar population synthesis code and the two-component dust model used to compute the emission of starlight and its transfer through the ISM in galaxies. Then, in Section 2.2, we present our model to compute the spectral energy distribution of the infrared emission from dust. We calibrate this model using a sample of 107 nearby star-forming galaxies observed by *IRAS* and *ISO*. In Section 2.3, we show examples of combined ultraviolet, optical and infrared spectral energy distributions of different types of star-forming galaxies.

2.1 Stellar emission and attenuation by dust

We use the latest version of the Bruzual & Charlot (2003) stellar population synthesis code to compute the light produced by stars in galaxies. This code predicts the spectral evolution of stellar populations at wavelengths from 91 Å to 160 μm and at ages between 1×10^5 and 2×10^{10} years, for different metallicities, initial mass functions (IMFs) and star formation histories. We use the most recent version of the code, which incorporates a new prescription by Marigo & Girardi (2007) for the TP-AGB evolution of low- and intermediate-mass stars. The main effect of this prescription is to improve the predicted near-infrared colours of intermediate-age stellar populations (Bruzual 2007; see also Charlot & Bruzual, in preparation). In all applications throughout this paper, we adopt the Galactic-disc IMF of Chabrier (2003).

We compute the attenuation of starlight by dust using the simple, angle-averaged model of Charlot & Fall (2000). This accounts for the fact that stars are born in dense molecular clouds, which dissipate typically on a timescale $t_0 \sim 10^7$ yr. Thus the emission from stars younger than t_0 is more attenuated than that from older stars. Following Charlot & Fall (2000), we express the luminosity per unit wavelength emerging at time t from a galaxy as

$$L_\lambda(t) = \int_0^t dt' \psi(t-t') S_\lambda(t') e^{-\hat{\tau}_\lambda(t')}, \quad (1)$$

where $\psi(t-t')$ is the star formation rate at time $t-t'$, $S_\lambda(t')$ is the luminosity per unit wavelength per unit mass emitted by a stellar generation of age t' , and $\hat{\tau}_\lambda(t')$ is the ‘effective’ absorption optical depth of the dust seen by stars of age t'

(i.e. averaged over photons emitted in all directions by stars in all locations within the galaxy). The time dependence of $\hat{\tau}_\lambda$ reflects the different attenuation affecting young and old stars in galaxies,

$$\hat{\tau}_\lambda(t') = \begin{cases} \hat{\tau}_\lambda^{\text{BC}} + \hat{\tau}_\lambda^{\text{ISM}} & \text{for } t' \leq t_0, \\ \hat{\tau}_\lambda^{\text{ISM}} & \text{for } t' > t_0. \end{cases} \quad (2)$$

Here $\hat{\tau}_\lambda^{\text{BC}}$ is the effective absorption optical depth of the dust in stellar birth clouds and $\hat{\tau}_\lambda^{\text{ISM}}$ that in the ambient ISM. We also adopt the prescription of Charlot & Fall (2000) to compute the emergent luminosities $L_{\text{H}\alpha}(t)$ and $L_{\text{H}\beta}(t)$ of the Hα ($\lambda = 6563$ Å) and Hβ ($\lambda = 4861$ Å) Balmer lines of hydrogen produced by stars in the birth clouds. This assumes case B recombination and includes the possible absorption of ionising photons by dust before they ionise hydrogen.

The shape of the effective absorption curve depends on the combination of the optical properties and spatial distribution of the dust. We adopt the following dependence of $\hat{\tau}_\lambda^{\text{BC}}$ and $\hat{\tau}_\lambda^{\text{ISM}}$ on wavelength:

$$\hat{\tau}_\lambda^{\text{BC}} = (1 - \mu) \hat{\tau}_V (\lambda/5500 \text{ Å})^{-1.3}, \quad (3)$$

$$\hat{\tau}_\lambda^{\text{ISM}} = \mu \hat{\tau}_V (\lambda/5500 \text{ Å})^{-0.7}, \quad (4)$$

where $\hat{\tau}_V$ is the total effective V-band absorption optical depth of the dust seen by young stars inside birth clouds, and $\mu = \hat{\tau}_V^{\text{ISM}} / (\hat{\tau}_V^{\text{BC}} + \hat{\tau}_V^{\text{ISM}})$ is the fraction of this contributed by dust in the ambient ISM. The dependence of $\hat{\tau}_\lambda^{\text{ISM}}$ on $\lambda^{-0.7}$ is well constrained by the observed relation between ratio of far-infrared to ultraviolet luminosity and ultraviolet spectral slope for nearby starburst galaxies (see Charlot & Fall 2000). The dependence of $\hat{\tau}_\lambda^{\text{BC}}$ on wavelength is less constrained by these observations, because stellar birth clouds tend to be optically thick, and hence, stars in these clouds contribute very little to the emergent radiation (except in the emission lines). For simplicity, Charlot & Fall (2000) adopt $\hat{\tau}_\lambda^{\text{BC}} \propto \lambda^{-0.7}$ by analogy with $\hat{\tau}_\lambda^{\text{ISM}}$. We adopt here a slightly steeper dependence, $\hat{\tau}_\lambda^{\text{BC}} \propto \lambda^{-1.3}$ (equation 3), which corresponds to the middle range of the optical properties of dust grains between the Milky Way, the Large and the Small Magellanic Clouds (see section 4 of Charlot & Fall 2000). This choice is motivated by the fact that giant molecular clouds can be assimilated to foreground shells when attenuating the light from newly born stars. In this case, the effective absorption curve should reflect the actual optical properties of dust grains. We emphasise that the dependence of $\hat{\tau}_\lambda^{\text{BC}}$ on wavelength has a negligible influence on the emergent ultraviolet and optical continuum radiation. It affects mainly the attenuation of emission lines in galaxies with large $\hat{\tau}_V^{\text{BC}} / \hat{\tau}_V^{\text{ISM}}$ and hence small μ (Section 3.4.2 below; see also Wild et al. 2007).

The fraction of stellar radiation absorbed by dust in the stellar birth clouds and in the ambient ISM is reradiated in the infrared. We write the total luminosity absorbed and reradiated by dust as the sum

$$L_d^{\text{tot}}(t) = L_d^{\text{BC}}(t) + L_d^{\text{ISM}}(t), \quad (5)$$

where

$$L_d^{\text{BC}}(t) = \int_0^\infty d\lambda \left(1 - e^{-\hat{\tau}_\lambda^{\text{BC}}}\right) \int_0^{t_0} dt' \psi(t-t') S_\lambda(t') \quad (6)$$

is the total infrared luminosity contributed by dust in the birth clouds, and

$$L_d^{\text{ISM}}(t) = \int_0^\infty d\lambda \left(1 - e^{-\tau_\lambda^{\text{ISM}}}\right) \int_{t_0}^t dt' \psi(t - t') S_\lambda(t') \quad (7)$$

is the total infrared luminosity contributed by dust in the ambient ISM. For some purposes, it is also convenient to define the fraction of the total infrared luminosity contributed by the dust in the ambient ISM:

$$f_\mu(t) \equiv L_d^{\text{ISM}}(t)/L_d^{\text{tot}}(t). \quad (8)$$

This depends on the total effective *V*-band absorption optical depth of the dust, τ_V , the fraction μ of this contributed by dust in the ambient ISM, and the star formation history (and IMF) determining the relative proportion of young and old stars in the galaxy.

2.2 Infrared emission of the dust

We now present a simple but physically motivated prescription to compute the spectral distribution of the energy reradiated by dust in the infrared (i.e., the distribution in wavelength of L_d^{BC} and L_d^{ISM}). By construction, the infrared emission computed in this way can be related to the emission at shorter wavelengths using equations (1)–(7) above.

2.2.1 Components of infrared emission

The infrared emission from galaxies is generally attributed to three main constituents of interstellar dust: polycyclic aromatic hydrocarbons (PAHs), which produce strong emission features at wavelengths between 3 and 20 μm ; ‘very small grains’ (with sizes typically less than 0.01 μm), which are stochastically heated to high temperatures by the absorption of single ultraviolet photons; and ‘big grains’ (with sizes typically between 0.01 and 0.25 μm), which are in thermal equilibrium with the radiation field. This picture arises from detailed models of the sizes and optical properties of dust grains and PAH molecules in the ISM of the Milky Way and other nearby galaxies (e.g., Mathis et al. 1977; Draine & Lee 1984; Leger & Puget 1984). Here, we build on the results from these studies to describe the different components of infrared emission in galaxies, without modelling in detail the physical properties of dust grains. As mentioned in Section 1, the motivation for this approach is to build a model simple enough to derive statistical constraints on the star formation and dust properties of large samples of observed galaxies, based on consistent fits of the ultraviolet, optical and infrared emission. We describe the different components of infrared emission in our model as follows:

(i) *PAH and near-infrared continuum emission.* The mid-infrared spectra of most normal star-forming galaxies are dominated by strong emission features at 3.3, 6.2, 7.7, 8.6, 11.3 and 12.7 μm . Although still uncertain, the carriers of these features are generally accepted to be PAH molecules transiently excited to high internal energy levels after the absorption of single ultraviolet photons (Leger & Puget 1984; Allamandola et al. 1985; Leger et al. 1989; Allamandola et al. 1999). PAH emission tends to peak in the ‘photo-dissociation regions’ (PDRs) at the interface between ionised and molecular gas in the outskirts of H II regions, where PAH molecules can survive and transient heating is most efficient (e.g., Cesarsky et al. 1996;

Verstraete et al. 1996; Rapacioli et al. 2005). In these environments, the non-ionising ultraviolet radiation from young stars dominates the energy balance and can dissociate molecules such as H_2 and CO (see Hollenbach & Tielens 1997 for a review).

Observations with *ISO*/ISOPHOT of the mid-infrared spectra of 45 nearby, normal star-forming galaxies do not reveal any strong variation of the PAH emission spectrum with galaxy properties such as infrared colours and infrared-to-blue luminosity ratio (Helou et al. 2000). For simplicity, we adopt a fixed template spectrum to describe PAH emission in our model.¹ We use the mid-infrared spectrum of the photo-dissociation region in the prototypical Galactic star-forming region M17 SW extracted from the *ISO*/ISOCAM observations of Cesarsky et al. (1996) by Madden et al. (2006). The observed spectrum does not extend blueward of 5 μm . We extend it to include the 3.3 μm PAH emission feature using the Lorentzian profile parametrised by Verstraete et al. (2001), $F_\nu^{\text{Lorentz}} = f_0[1 + (x - x_0)^2/\sigma^2]^{-1}$, where $x = 1/\lambda$ is the wavenumber, $x_0 = 3039.1 \text{ cm}^{-1}$ the central wavenumber of the feature and $\sigma = 19.4 \text{ cm}^{-1}$ half the FWHM. We set the amplitude f_0 so that the luminosity of the 3.3 μm emission feature is 10 per cent of that of the 11.3 μm feature (the relative ratio found by Li & Draine 2001 for neutral PAHs). We write the spectral energy distribution of PAHs in our model

$$l_\lambda^{\text{PAH}} = L_\lambda^{\text{M17}} \left(\int_0^\infty d\lambda L_\lambda^{\text{M17}} \right)^{-1}, \quad (9)$$

where L_λ^{M17} is the adopted M17 spectral template, and l_λ^{PAH} is normalised to unit total energy.

The above *ISO*/ISOPHOT observations of a sample of 45 normal star-forming galaxies also reveal a component of near-infrared continuum emission characterised by a very high colour temperature ($\sim 1000 \text{ K}$) at wavelengths between 3 and 5 μm (Lu et al. 2003). This component accounts typically for at most a few percent of the total infrared luminosity, but it contributes significantly to the observed *Spitzer*/IRAC band fluxes at 3.6 and 4.5 μm . It is also present in the spectra of reflection nebulae (Sellgren et al. 1983) and in the diffuse cirrus emission of the Milky Way (Dwek et al. 1997; Flagey et al. 2006). The origin of this emission is still uncertain, and it could be related to the stochastic heating of PAH molecules or carbon grains (e.g. Flagey et al. 2006). Lu et al. (2003) find that the strength of this emission correlates well with that of PAH features in the spectra of the galaxies in their sample. In particular, the ratio of the continuum flux density at 4 μm to the mean flux density of the 7.7 μm PAH feature has a roughly constant value of 0.11.

To implement this component of near-infrared continuum emission associated to PAH emission in our model, we use a greybody (i.e. modified blackbody) function of the form (e.g., Hildebrand 1983)

¹ In reality, changes in PAH molecule size and ionisation state, variations in metallicity and contamination by an AGN could cause variations of up to 40 per cent in the relative strengths of some PAH emission features (Helou et al. 2000; Brandl et al. 2006; Smith et al. 2007; Galliano et al. 2007). We ignore this refinement here.

$$l_{\lambda}^{T_d} = \kappa_{\lambda} B_{\lambda}(T_d) \left[\int_0^{\infty} d\lambda \kappa_{\lambda} B_{\lambda}(T_d) \right]^{-1}, \quad (10)$$

where $B_{\lambda}(T_d)$ is the Planck function of temperature T_d , κ_{λ} is the dust mass absorption coefficient, and $l_{\lambda}^{T_d}$ is normalised to unit total energy. The dust mass absorption coefficient is usually approximated by a single power law of the form

$$\kappa_{\lambda} \propto \lambda^{-\beta}, \quad (11)$$

where β is the dust emissivity index. Models and observations of infrared to sub-millimetre dust emission and laboratory studies of carbonaceous and amorphous silicate grains suggest values of β in the range $1 \lesssim \beta \lesssim 2$, with some dependence on grain size and temperature (Andriesse 1974; Hildebrand 1983; Draine & Lee 1984; Reach et al. 1995; Agladze et al. 1996; Boulanger et al. 1996; Mennella et al. 1998; see also section 3.4 of Dunne & Eales 2001 and section 4 of Dale & Helou 2002 for discussions on the constraints on β). Typically, these studies favour $\beta \approx 1$ for small carbonaceous grains, which radiate most of their energy at mid-infrared wavelengths, and $\beta \approx 1.5 - 2$ for big silicate grains, which reach lower temperatures and radiate most of their energy at far-infrared and sub-millimeter wavelengths. We therefore adopt $\beta = 1$ in equation (11) to compute the near-infrared continuum emission in our model. We scale this emission so that the continuum flux density at $4 \mu\text{m}$ be 0.11 times the mean flux density of the $7.7 \mu\text{m}$ PAH feature (see above). We find that a temperature $T_d = 850 \text{ K}$ provides optimal fits to the observed spectral energy distributions of galaxies at wavelengths between 3 and $5 \mu\text{m}$ (see, e.g., Fig. 1).

(ii) *Mid-infrared continuum emission from hot dust.* In addition to PAH features, the mid-infrared spectra of star-forming galaxies (out to wavelengths $\lambda \sim 40 \mu\text{m}$) also include a component of smooth continuum emission. This component is generally attributed to a continuous distribution of small grains with very low heat capacity, which are stochastically heated to high temperatures by the absorption of single ultraviolet photons (e.g., Sellgren 1984). The accurate modelling of this emission would require the computation of temperature fluctuations of grains of different sizes and optical properties caused by the absorption of ultraviolet photons in different interstellar radiation fields (e.g. Purcell 1976; Aannestad & Kenyon 1979). For simplicity, in our model, we describe the ‘hot’ mid-infrared continuum emission as the sum of two greybodies (equation 10) of temperatures $T_d = 130$ and 250 K , with equal contributions to the total infrared luminosity,

$$l_{\lambda}^{\text{MIR}} = (l_{\lambda}^{250} + l_{\lambda}^{130}) \left[\int_0^{\infty} d\lambda (l_{\lambda}^{250} + l_{\lambda}^{130}) \right]^{-1}. \quad (12)$$

We find that these two temperatures reproduce in an optimal way the range of infrared colours of star-forming galaxies (see Section 2.2.2 below).

(iii) *Emission from grains in thermal equilibrium.* At far-infrared wavelengths, the emission from galaxies is generally dominated by dust grains in thermal equilibrium at low temperatures. The grain temperatures depend sensitively on the intensity of the interstellar radiation field. This is why the peak of the far-infrared spectral energy distribution of a galaxy is a good indicator of dust heating in the ISM.

We consider two types of grains in thermal equilibrium

in our model: warm grains, which can reside both in stellar birth clouds and in the ambient ISM, with characteristic temperatures T_{W}^{BC} and $T_{\text{W}}^{\text{ISM}}$, respectively; and cold grains, which can reside only in the ambient ISM, with characteristic temperature $T_{\text{C}}^{\text{ISM}}$. To account for the observed dispersion in the peak of the far-infrared emission of galaxies with different star formation activities, we allow the warm-grain temperature to vary between 30 and 60 K and the cold-grain temperature to vary between 15 and 25 K. We describe the emission from grains in thermal equilibrium using greybody spectra (equation 10) with emissivity index $\beta = 1.5$ for warm dust and $\beta = 2.0$ for cold dust (equation 11).

In summary, the infrared spectral energy distribution of stellar birth clouds in our model can be written

$$L_{\lambda, \text{d}}^{\text{BC}} = (\xi_{\text{PAH}}^{\text{BC}} l_{\lambda}^{\text{PAH}} + \xi_{\text{MIR}}^{\text{BC}} l_{\lambda}^{\text{MIR}} + \xi_{\text{W}}^{\text{BC}} l_{\lambda}^{T_{\text{W}}^{\text{BC}}}) (1 - f_{\mu}) L_{\text{d}}^{\text{tot}}, \quad (13)$$

where $L_{\text{d}}^{\text{tot}}$ is the total infrared luminosity reradiated by dust (equation 5), f_{μ} is the fraction of this contributed by the ambient ISM (equation 8), l_{λ}^{PAH} , l_{λ}^{MIR} and $l_{\lambda}^{T_{\text{W}}^{\text{BC}}}$ are computed using equations (9), (12) and (10), and $\xi_{\text{PAH}}^{\text{BC}}$, $\xi_{\text{MIR}}^{\text{BC}}$ and $\xi_{\text{W}}^{\text{BC}}$ are the relative contributions by PAHs, the hot mid-infrared continuum and grains in thermal equilibrium to the total infrared luminosity of the birth clouds. These satisfy the condition

$$\xi_{\text{PAH}}^{\text{BC}} + \xi_{\text{MIR}}^{\text{BC}} + \xi_{\text{W}}^{\text{BC}} = 1. \quad (14)$$

Similarly, the infrared spectral energy distribution of the ambient ISM can be written

$$L_{\lambda, \text{d}}^{\text{ISM}} = (\xi_{\text{PAH}}^{\text{ISM}} l_{\lambda}^{\text{PAH}} + \xi_{\text{MIR}}^{\text{ISM}} l_{\lambda}^{\text{MIR}} + \xi_{\text{W}}^{\text{ISM}} l_{\lambda}^{T_{\text{W}}^{\text{ISM}}} + \xi_{\text{C}}^{\text{ISM}} l_{\lambda}^{T_{\text{C}}^{\text{ISM}}}) f_{\mu} L_{\text{d}}^{\text{tot}}, \quad (15)$$

where l_{λ}^{PAH} , l_{λ}^{MIR} , $l_{\lambda}^{T_{\text{W}}^{\text{ISM}}}$ and $l_{\lambda}^{T_{\text{C}}^{\text{ISM}}}$ are computed using equations (9), (12) and (10), and $\xi_{\text{PAH}}^{\text{ISM}}$, $\xi_{\text{MIR}}^{\text{ISM}}$, $\xi_{\text{W}}^{\text{ISM}}$ and $\xi_{\text{C}}^{\text{ISM}}$ are the relative contributions by PAHs, the hot mid-infrared continuum and warm and cold grains in thermal equilibrium to the total infrared luminosity of the ISM. These satisfy the condition

$$\xi_{\text{PAH}}^{\text{ISM}} + \xi_{\text{MIR}}^{\text{ISM}} + \xi_{\text{W}}^{\text{ISM}} + \xi_{\text{C}}^{\text{ISM}} = 1. \quad (16)$$

In practice, we can fix the shape of the mid-infrared spectral energy distribution of the ambient ISM in our model to keep the number of adjustable parameters as small as possible. This is justified by the fact that the intensity of the average radiation field heating dust in the diffuse ISM of normal galaxies is roughly constant (e.g., Helou 1986). Moreover, sophisticated models of dust emission by Li & Draine (2001) and Draine & Li (2007) suggest that even large variations of the intensity of the interstellar radiation field have only a small influence on the overall shape of the diffuse mid-infrared spectral energy distribution. In these conditions, we can appeal for example to observations of high-Galactic-latitude (cirrus) dust emission in the Milky Way to constrain the mid-infrared spectral energy distribution of the ambient ISM in our model. In Fig. 1, we show the model spectral energy distribution $L_{\lambda, \text{d}}^{\text{ISM}}$ (in black) computed using equation (15) that best fits the mean Galactic cirrus emission observed by the *Cosmic Background Explorer*/Diffuse Infrared Background Experiment (*COBE*/DIRBE) at wavelengths between 3.5 and $240 \mu\text{m}$ (Dwek et al. 1997). The blue lines

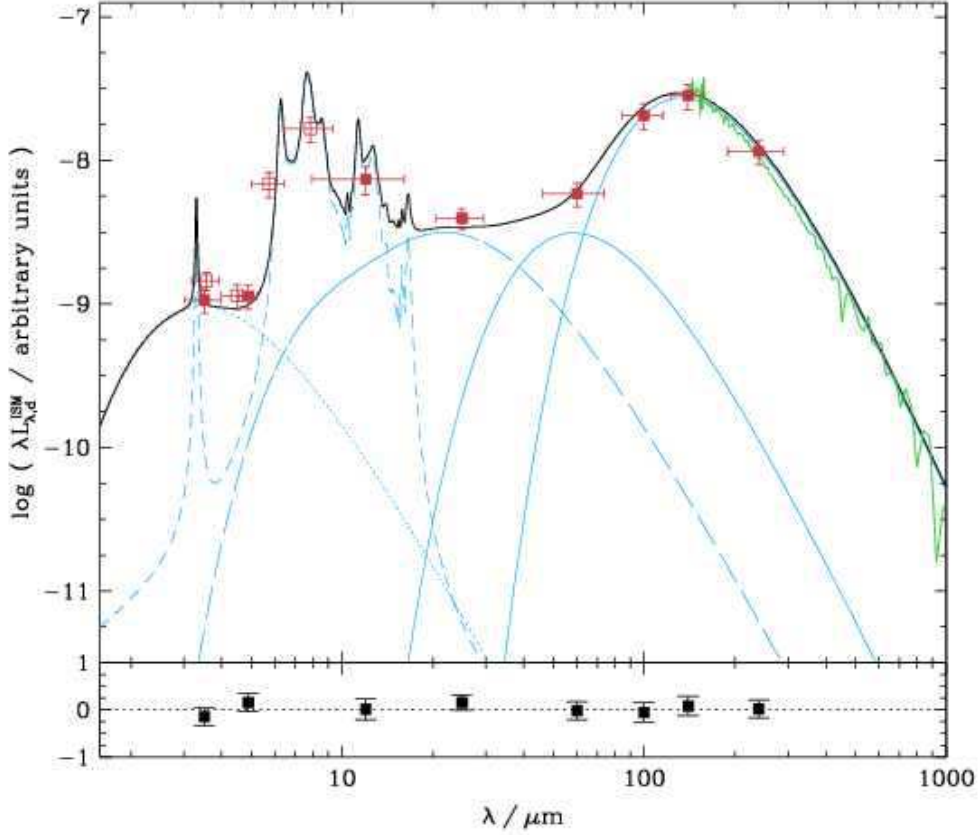


Figure 1. Best model fit (in black) to the observed mean spectral energy distribution of the Galactic cirrus emission. The model was computed using equation (15) and the parameters listed in equation (17). The red filled squares are the *COBE*/DIRBE observations of Dwek et al. (1997). Also shown for reference are the *Spitzer*/IRAC observations of Flagey et al. (2006, red open squares) and the *COBE*/FIRAS observations of Dwek et al. (1997, green line). The blue lines show the decomposition of the model in its different components (see Section 2.2): near-infrared continuum (*dotted*); PAHs (*short-dashed*); hot mid-infrared continuum (*long-dashed*) and warm and cold grains in thermal equilibrium (*solid*). The fit residuals $(L_{\lambda}^{\text{obs}} - L_{\lambda}^{\text{mod}})/L_{\lambda}^{\text{obs}}$, where L_{λ}^{obs} and L_{λ}^{mod} are the observed and model fluxes in a given photometric band, are shown at the bottom.

show the different components of the best-fit model, with parameters

$$\begin{aligned}
 \xi_{\text{PAH}}^{\text{ISM}} &= 0.22 \\
 \xi_{\text{MIR}}^{\text{ISM}} &= 0.11 \\
 \xi_{\text{W}}^{\text{ISM}} &= 0.07 \\
 \xi_{\text{C}}^{\text{ISM}} &= 0.60 \\
 T_{\text{W}}^{\text{ISM}} &= 45 \text{ K} \\
 T_{\text{C}}^{\text{ISM}} &= 18 \text{ K}.
 \end{aligned} \tag{17}$$

For reference, we include in Fig. 1 additional observations of the mean Galactic cirrus emission obtained with *Spitzer*/IRAC at wavelengths 3.6, 4.5, 5.8 and 8.0 μm (Flagey et al. 2006) and with the *COBE*/Far-Infrared Absolute Spectrophotometer (FIRAS) at wavelengths between 140 and 1000 μm (Dwek et al. 1997). The model reproduces these observations remarkably well, even though they were not included in the fit.

We use the constraints of Fig. 1 to fix the mid-infrared spectral energy distribution of the ambient ISM and reduce the number of adjustable parameters in our model. Specifically, we fix the relative contributions by PAHs, the hot

mid-infrared continuum and warm grains in thermal equilibrium to the total infrared luminosity of the ambient ISM (i.e. the relative ratios of $\xi_{\text{PAH}}^{\text{ISM}}$, $\xi_{\text{MIR}}^{\text{ISM}}$ and $\xi_{\text{W}}^{\text{ISM}}$) to their values of equation (17), and we keep $\xi_{\text{C}}^{\text{ISM}}$ and $T_{\text{C}}^{\text{ISM}}$ as adjustable parameters. Thus, for a given contribution $\xi_{\text{C}}^{\text{ISM}}$ by cold grains in thermal equilibrium to the total infrared luminosity of the ambient ISM, the contributions by PAHs, the hot mid-infrared continuum and warm grains in thermal equilibrium are $\xi_{\text{PAH}}^{\text{ISM}} = 0.550(1 - \xi_{\text{C}}^{\text{ISM}})$, $\xi_{\text{MIR}}^{\text{ISM}} = 0.275(1 - \xi_{\text{C}}^{\text{ISM}})$ and $\xi_{\text{W}}^{\text{ISM}} = 0.175(1 - \xi_{\text{C}}^{\text{ISM}})$, respectively.

The total spectral energy distribution of a galaxy in our model is computed as the sum

$$L_{\lambda,d}^{\text{tot}} = L_{\lambda,d}^{\text{BC}} + L_{\lambda,d}^{\text{ISM}}, \tag{18}$$

where $L_{\lambda,d}^{\text{BC}}$ and $L_{\lambda,d}^{\text{ISM}}$ are given by equations (13) and (15). For some purposes, it is also convenient to define the global contribution by a specific dust component, including stellar birth clouds and the ambient ISM, to the total infrared luminosity of a galaxy. This can be written

$$\xi_{\text{PAH}}^{\text{tot}} = \xi_{\text{PAH}}^{\text{BC}} (1 - f_{\mu}) + 0.550 (1 - \xi_{\text{C}}^{\text{ISM}}) f_{\mu}, \tag{19}$$

$$\xi_{\text{MIR}}^{\text{tot}} = \xi_{\text{MIR}}^{\text{BC}} (1 - f_{\mu}) + 0.275 (1 - \xi_{\text{C}}^{\text{ISM}}) f_{\mu}, \quad (20)$$

$$\xi_{\text{W}}^{\text{tot}} = \xi_{\text{W}}^{\text{BC}} (1 - f_{\mu}) + 0.175 (1 - \xi_{\text{C}}^{\text{ISM}}) f_{\mu}, \quad (21)$$

$$\xi_{\text{C}}^{\text{tot}} = \xi_{\text{C}}^{\text{ISM}} f_{\mu}, \quad (22)$$

for PAHs, the hot mid-infrared continuum and warm and cold dust in thermal equilibrium, respectively.

We compute luminosity densities in any filter from $L_{\lambda, \text{d}}^{\text{tot}}$ using the general formula

$$L_{\nu}^{\lambda_0} = C_{\nu_0} \frac{\int d\nu \nu^{-1} L_{\nu} R_{\nu}}{\int d\nu \nu^{-1} C_{\nu} R_{\nu}} = \frac{\lambda_0^2}{c} C_{\lambda_0} \frac{\int d\lambda \lambda R_{\lambda}}{\int d\lambda C_{\lambda} R_{\lambda}}, \quad (23)$$

where

$$\lambda_0 = \frac{\int d\lambda \lambda R_{\lambda}}{\int d\lambda R_{\lambda}} \quad (24)$$

is the effective wavelength of the filter of response R_{λ} (R_{ν}), and the calibration spectrum C_{λ} (C_{ν}) depends on the photometric system. For the AB system, C_{ν} is fixed at 3631 Jy, implying $C_{\lambda} \propto \lambda^{-2}$ (Oke & Gunn 1983). For the *IRAS*, *ISO*/ISOCAM and *Spitzer*/IRAC photometric systems, the convention is to use $\nu C_{\nu} = \lambda C_{\lambda} = \text{constant}$, and hence, $C_{\lambda} \propto \lambda^{-1}$ (see Beichman et al. 1988; Blommaert et al. 2003; Reach et al. 2005, and also the IRAC Data Handbook²). The *Spitzer*/MIPS system was calibrated using a blackbody spectrum of temperature 10,000 K, such that $C_{\lambda} = B_{\lambda}(10,000 \text{ K})$ (MIPS Data Handbook³). In Fig. 2, we show an example of infrared spectral energy distribution $L_{\lambda, \text{d}}^{\text{tot}}$ computed using our model, for parameter values typical of normal star-forming galaxies (equation 25 below). As we shall see in Section 2.2.2, this parameterisation of infrared galaxy spectra allows us to account for the full range of observed colours of star-forming galaxies.

2.2.2 Comparison with observed infrared colours

To test how well our model can reproduce the observed infrared colours of galaxies in a wide range of star formation histories, we appeal to a sample of 157 nearby galaxies compiled by Elbaz et al. (2002), for which *IRAS* and *ISO*/ISOCAM observations are available from Boselli et al. (1998), Roussel et al. (2001), Laurent et al. (2000) and Dale et al. (2000). The galaxies in this sample span wide ranges of morphologies, absolute infrared luminosities, infrared-to-blue luminosity ratios and infrared colours (see Elbaz et al. 2002 for more detail). For nearby galaxies, the flux density collected by the ISOCAM *LW2* (6.75 μm) filter, $F_{\nu}^{6.75}$, tends to be dominated by the PAH emission features at 6.2, 7.7 and 8.6 μm . The *IRAS* 12- μm flux density F_{ν}^{12} captures the PAH emission at 11.3 and 12.7 μm and the mid-infrared continuum emission from hot dust. The ISO-CAM *LW3* (15 μm) and the *IRAS* 25- μm flux densities, F_{ν}^{15} and F_{ν}^{25} , reflect primarily the mid-infrared continuum emission from hot dust. At longer wavelengths, the *IRAS* 60- μm flux density F_{ν}^{60} samples the emission from warm grains in thermal equilibrium in star-forming clouds, and the *IRAS* 100- μm flux density F_{ν}^{100} that from colder grains in thermal equilibrium in the ambient interstellar medium.

To test our model, we require photometric observations in all these filters. This reduces the sample to 107 galaxies. For the purpose of comparisons between our (angle-averaged) model and observations, we neglect possible anisotropies and equate flux ratios at all wavelengths to the corresponding luminosity ratios.

In Figs. 3 and 4, we show the locations of these galaxies in various infrared colour-colour diagrams (black crosses). Fig. 3 shows $L_{\nu}^{60}/L_{\nu}^{100}$ as a function of $L_{\nu}^{12}/L_{\nu}^{25}$ (*IRAS* colours), while Fig. 4 shows $L_{\nu}^{15}/L_{\nu}^{60}$ as a function of $L_{\nu}^{6.75}/L_{\nu}^{15}$ (*ISO* colours). The well-known correlations between the different infrared colours of galaxies illustrated by Figs. 3 and 4 suggest that the different contributors to the total infrared emission are related to one another. These relations are generally interpreted as sequences in the overall star formation activity and dust heating (e.g. Helou 1986; Dale et al. 2001). Quiescent star-forming galaxies with strong PAH emission and cool ambient-ISM dust tend to have high $L_{\nu}^{12}/L_{\nu}^{25}$, $L_{\nu}^{6.75}/L_{\nu}^{15}$ and $L_{\nu}^{15}/L_{\nu}^{60}$ and low $L_{\nu}^{60}/L_{\nu}^{100}$. In contrast, actively star-forming galaxies, in which the mid-infrared emission is dominated by continuum radiation by hot dust and the far-infrared emission by warm dust in star-forming regions, tend to have low $L_{\nu}^{12}/L_{\nu}^{25}$, $L_{\nu}^{6.75}/L_{\nu}^{15}$ and $L_{\nu}^{15}/L_{\nu}^{60}$ and high $L_{\nu}^{60}/L_{\nu}^{100}$.

We now use these observations to explore the influence of each parameter of our model on the various infrared colours. We explore the effect of varying a single parameter at a time, keeping all the other parameters fixed at ‘standard’ values. After some experimentation, we adopted the following standard parameters (corresponding to the model shown in Fig. 2):

$$\begin{aligned} f_{\mu} &= 0.60 \\ \xi_{\text{PAH}}^{\text{BC}} &= 0.05 \\ \xi_{\text{MIR}}^{\text{BC}} &= 0.15 \\ \xi_{\text{W}}^{\text{BC}} &= 0.80 \\ \xi_{\text{C}}^{\text{ISM}} &= 0.80 \\ T_{\text{W}}^{\text{BC}} &= 48 \text{ K} \\ T_{\text{C}}^{\text{ISM}} &= 22 \text{ K}. \end{aligned} \quad (25)$$

These values allow the standard model to match roughly the observed typical (i.e. median) infrared colours of nearby star-forming galaxies in Figs. 3 and 4 (green circle). Each panel of Figs. 3 and 4 shows the effect of varying one parameter of the model, with the other parameters held fixed at their standard values.⁴ We can summarise the role of each parameter as follows.

Fraction of total infrared luminosity contributed by dust in the ambient ISM. The dominant effect of increasing f_{μ} is to increase the contribution to the total infrared luminosity by cold dust. This raises the infrared luminosity around 100 μm (Fig. 2), causing $L_{\nu}^{60}/L_{\nu}^{100}$ and even $L_{\nu}^{15}/L_{\nu}^{60}$ to decrease (Figs. 3a and 4a). In addition, a larger f_{μ} leads to an increase in $L_{\nu}^{12}/L_{\nu}^{25}$ and $L_{\nu}^{6.75}/L_{\nu}^{15}$, due to the increased contribution

⁴ In practice, an increase in any of $\xi_{\text{PAH}}^{\text{BC}}$, $\xi_{\text{MIR}}^{\text{BC}}$ and $\xi_{\text{W}}^{\text{BC}}$ will be accompanied by a drop in the other two fractions by virtue of equation (14). Likewise, an increase in $\xi_{\text{C}}^{\text{ISM}}$ implies a drop in the sum $\xi_{\text{PAH}}^{\text{ISM}} + \xi_{\text{MIR}}^{\text{ISM}} + \xi_{\text{W}}^{\text{ISM}}$ (equation 16). When exploring such variations, we keep the relative ratios of the unexplored fractions fixed.

² <http://ssc.spitzer.caltech.edu/irac/dh/>

³ <http://ssc.spitzer.caltech.edu/mips/dh/>

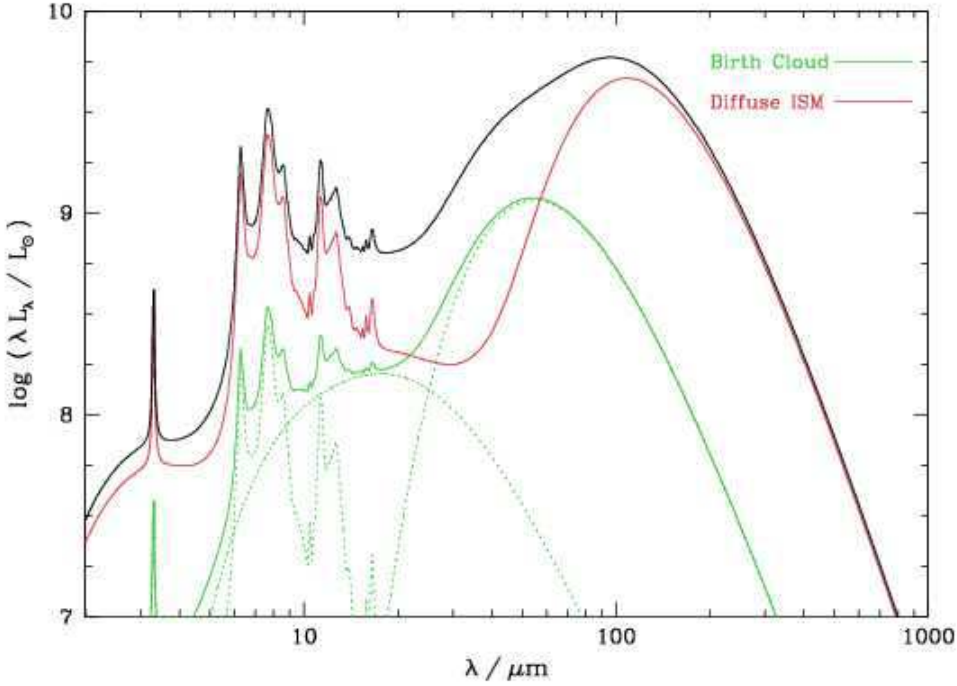


Figure 2. Example of infrared spectral energy distribution computed using the model presented in Section 2.2.1, for ‘standard’ values of the parameters (equation 25): $f_{\mu} = 0.6$, $\xi_{\text{PAH}}^{\text{BC}} = 0.05$, $\xi_{\text{MIR}}^{\text{BC}} = 0.15$, $\xi_{\text{W}}^{\text{BC}} = 0.80$, $T_{\text{W}}^{\text{BC}} = 48$ K, $\xi_{\text{C}}^{\text{ISM}} = 0.8$ and $T_{\text{C}}^{\text{ISM}} = 22$ K. The black curve shows the total infrared spectrum. The green solid curve shows the contribution by dust in the stellar birth clouds, and the green dashed curves the breakdown of this contribution in different components: PAHs, mid-infrared continuum and warm dust in thermal equilibrium. The red curve shows the contribution by dust in the ambient ISM. The total luminosity is $L_{\text{d}}^{\text{tot}} = 10^{10} L_{\odot}$ (equations 13, 15 and 18).

by PAH emission features (which dominate the mid-infrared emission of the ISM) to the total mid-infrared emission.

Contribution by cold dust in thermal equilibrium to the infrared emission from the ambient ISM. Increasing $\xi_{\text{C}}^{\text{ISM}}$ causes $L_{\nu}^{12}/L_{\nu}^{25}$ and $L_{\nu}^{6.75}/L_{\nu}^{15}$ to decrease in Figs. 3b and 4b, because of the corresponding drop in PAH emission from the ambient ISM (see footnote 4). Also, both $L_{\nu}^{15}/L_{\nu}^{60}$ and $L_{\nu}^{60}/L_{\nu}^{100}$ decrease because of the larger contribution by cold dust to the 60 μm flux, and even more so to the 100 μm flux.

Contribution by PAHs to the infrared emission from stellar birth clouds. Increasing $\xi_{\text{PAH}}^{\text{BC}}$ raises the contribution by PAH features to $L_{\nu}^{6.75}$ and L_{ν}^{12} , and to a lesser extent L_{ν}^{15} (Fig. 2). This leads to a marked increase in $L_{\nu}^{6.75}/L_{\nu}^{15}$ and $L_{\nu}^{12}/L_{\nu}^{25}$ and a milder one in $L_{\nu}^{15}/L_{\nu}^{60}$ in Figs. 3c and 4c. The slight decrease in $L_{\nu}^{60}/L_{\nu}^{100}$ when $\xi_{\text{PAH}}^{\text{BC}}$ increases in Fig. 3c is caused by the associated drop in $\xi_{\text{BG}}^{\text{BC}}$ (footnote 4).

Contribution by the hot mid-infrared continuum to the infrared emission from stellar birth clouds. The main effect of increasing $\xi_{\text{MIR}}^{\text{BC}}$ is to make L_{ν}^{15} and L_{ν}^{25} larger (Fig. 2). This causes a drop in $L_{\nu}^{12}/L_{\nu}^{25}$ and $L_{\nu}^{6.75}/L_{\nu}^{15}$, while $L_{\nu}^{15}/L_{\nu}^{60}$ increases (Figs. 3d and 4d). The slight decrease in $L_{\nu}^{60}/L_{\nu}^{100}$ when $\xi_{\text{MIR}}^{\text{BC}}$ increases in Fig. 3c is again caused by the associated drop in $\xi_{\text{BG}}^{\text{BC}}$ (footnote 4).

Contribution by warm dust in thermal equilibrium to the infrared emission from stellar birth clouds. Increasing $\xi_{\text{W}}^{\text{BC}}$ makes L_{ν}^{60} larger, and to a lesser extent also L_{ν}^{25} and L_{ν}^{100} (Fig. 2). Remarkably, this causes $L_{\nu}^{12}/L_{\nu}^{25}$ to drop and

$L_{\nu}^{60}/L_{\nu}^{100}$ to rise in Fig. 3e, almost along the observational relation. In Fig. 4e, an increase in $\xi_{\text{W}}^{\text{BC}}$ makes L_{ν}^{15} smaller (because of the associated drop in $\xi_{\text{MIR}}^{\text{BC}}$; see footnote 4), and hence, $L_{\nu}^{15}/L_{\nu}^{60}$ smaller and $L_{\nu}^{6.75}/L_{\nu}^{15}$ larger.

Equilibrium temperature of warm dust in stellar birth clouds. Increasing T_{W}^{BC} across the range from 30 to 60 K moves the wavelength of peak luminosity of dust in thermal equilibrium in the stellar birth clouds roughly from 70 to 40 μm . This causes $L_{\nu}^{12}/L_{\nu}^{25}$ to drop and $L_{\nu}^{60}/L_{\nu}^{100}$ to rise in Fig. 3f. In Fig. 4f, the effects on $L_{\nu}^{6.75}/L_{\nu}^{15}$ and $L_{\nu}^{15}/L_{\nu}^{60}$ are negligible.

Equilibrium temperature of cold dust in the ambient ISM (not shown). The most significant effect of increasing $T_{\text{C}}^{\text{ISM}}$ at fixed $\xi_{\text{C}}^{\text{ISM}}$ in Figs. 3 and 4 is a small rise in $L_{\nu}^{60}/L_{\nu}^{100}$ caused by a blue shift of the peak infrared luminosity of cold dust in the ambient ISM (from about 140 to 80 μm as $T_{\text{C}}^{\text{ISM}}$ increases from 15 to 25 K). Variations in $T_{\text{C}}^{\text{ISM}}$ also have a significant influence on the emission redward of 100 μm .

The green lines in Figs. 3 and 4 show that the extremities of the observational relations between the different infrared colours of galaxies cannot be reached by varying a single model parameter at a time. This suggests that variations in the different dust components of galaxies are related to each other. However, we have checked that the properties of every galaxy in Figs. 3 and 4 could be reproduced with at least one combination of parameters of our model. We illustrate this by showing two models lying at the ends of

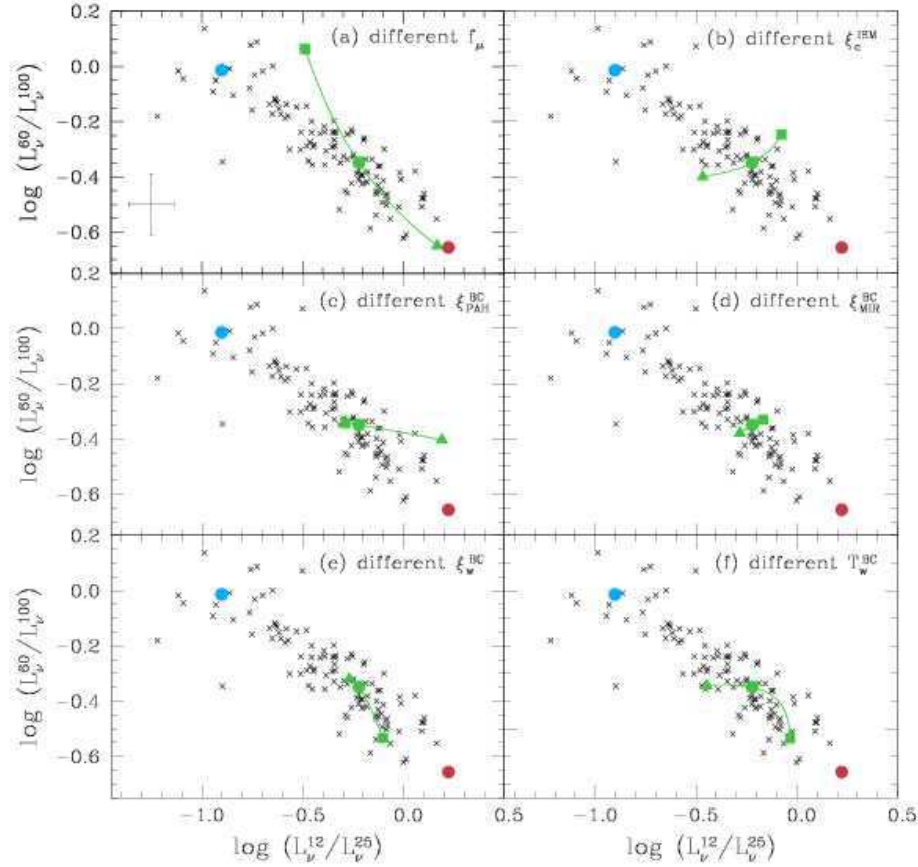


Figure 3. Ratio of 60- μm to 100- μm *IRAS* luminosity density plotted against ratio of 12- μm to 25- μm *IRAS* luminosity density. The data points in all panels (black crosses) are from the Elbaz et al. (2002) sample discussed in Section 2.2 (typical measurement errors are indicated in the upper left panel). In each panel, the green line shows the effect of varying one parameter of the model from the lower end of the range (square) to the standard value (green circle) to the upper end of the range (triangle), with all other parameters fixed at their standard values: (a) fraction of total infrared luminosity contributed by dust in the ambient ISM, $f_\mu = 0.05, 0.50$ and 0.95 ; (b) contribution by cold dust in thermal equilibrium to the infrared luminosity of the ambient ISM, $\xi_c^{\text{ISM}} = 0.50, 0.80, 1.0$; (c) contribution by PAHs to the infrared luminosity of stellar birth clouds, $\xi_{\text{PAH}}^{\text{BC}} = 0.00, 0.05$ and 0.50 ; (d) contribution by the hot mid-infrared continuum to the infrared luminosity of stellar birth clouds, $\xi_{\text{MIR}}^{\text{BC}} = 0.00, 0.15$ and 0.50 ; (e) contribution by warm dust in thermal equilibrium to the infrared luminosity of stellar birth clouds, $\xi_W^{\text{BC}} = 0.15, 0.80$ and 0.95 ; (f) equilibrium temperature of warm dust in stellar birth clouds, $T_W^{\text{BC}} = 30, 48$ and 60 K. In all panels, the red circle corresponds to the same quiescent model galaxy dominated by cold dust emission, while the blue circle corresponds to an actively star-forming galaxy dominated hot dust emission (see Table 1 and Section 2.2 for a description of these models).

the observational relations: a ‘cold’ infrared spectrum characteristic of a quiescent galaxy with little star formation (red circle); and a ‘hot’ infrared spectrum characteristic of an actively star-forming, starburst galaxy (blue circle). The parameters of these models are listed in Table 1. We emphasise that these are not unique sets of parameters optimised to fit specific galaxy spectral energy distributions. Rather, they are examples of how the colours in those regions of the diagrams can be reproduced using our model.

Figs. 3 and 4 allow us to draw some general conclusions about the influence of the various parameters of our model on the observed infrared colours of galaxies. For example, as expected from Fig. 2, the L_ν^{60}/L_ν^{100} colour appears to be controlled primarily by the fraction f_μ of total infrared luminosity contributed by dust in the ambient ISM and the properties of dust in thermal equilibrium: the relative con-

tribution ξ_c^{ISM} by cold dust to the infrared luminosity of the ambient ISM (and the temperature T_c^{ISM} of this dust) and the relative contribution ξ_W^{BC} by warm dust to the infrared luminosity of stellar birth clouds (and the temperature T_W^{BC} of this dust). These parameters also have distinct effects on the mid-infrared colours L_ν^{12}/L_ν^{25} , $L_\nu^{6.75}/L_\nu^{15}$ and L_ν^{15}/L_ν^{60} , indicating that they can be constrained independently from fits of extended infrared spectral energy distributions. The mid-infrared colours are primarily controlled by the different components of hot dust: the relative contributions $\xi_{\text{PAH}}^{\text{BC}}$ and $\xi_{\text{MIR}}^{\text{BC}}$ of PAHs and the hot mid-infrared continuum to the infrared luminosity of stellar birth clouds, and the contribution by PAHs to the infrared luminosity of the ambient ISM, which is controlled indirectly by ξ_c^{ISM} . In Section 3 below, we show how well these various model parameters can

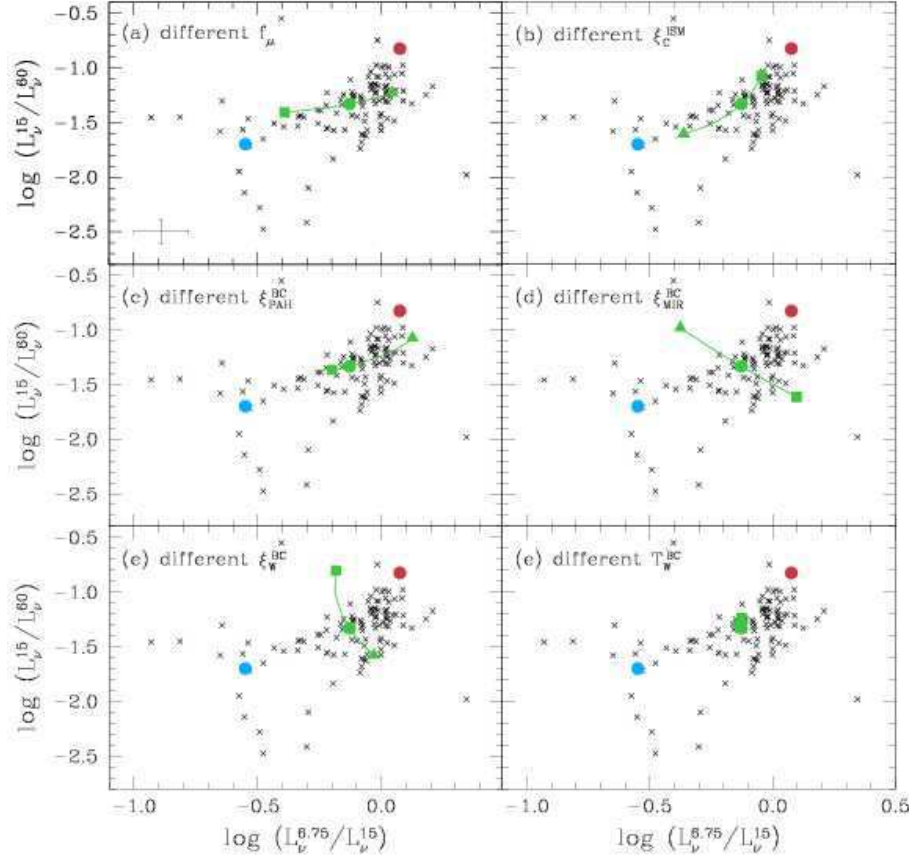


Figure 4. Ratio of 15- μ m to 60- μ m *ISO* and *IRAS* luminosity density plotted against ratio of 6.75- μ m to 15- μ m *ISO* luminosity density. The data points in all panels (black crosses) are from the Elbaz et al. (2002) sample discussed in Section 2.2. In each panel, the green line shows the effect of varying one parameter of the model from the lower end of the range (square) to the standard value (green circle) to the upper end of the range (triangle), with all other parameters fixed at their standard values. The models are the same as in Fig. 3. In all panels, the red circle corresponds to the same quiescent model galaxy dominated by cold dust emission, while the blue circle corresponds to an actively star-forming galaxy dominated hot dust emission (see Table 1 and Section 2.2 for a description of these models).

Table 1. Parameters of the ‘standard’, ‘cold’ and ‘hot’ models plotted in Figs. 3 and 4.

Model	‘cold’	‘standard’	‘hot’
f_μ	0.75	0.60	0.20
ξ_c^{ISM}	0.75	0.80	0.90
$\xi_{\text{PAH}}^{\text{BC}}$	0.45	0.05	0.01
$\xi_{\text{MIR}}^{\text{BC}}$	0.15	0.15	0.09
ξ_W^{BC}	0.40	0.80	0.95
T_W^{BC} (K)	40	48	55
T_c^{ISM} (K)	18	22	25

2.2.3 Constraints on dust mass

It is also of interest to derive constraints on the dust mass in galaxies. The mass $M_d(T_d)$ in dust grains in thermal equilibrium at the temperature T_d can be estimated from the far-infrared radiation $L_\lambda^{T_d}$ of these grains using the formula (Hildebrand 1983)

$$L_\lambda^{T_d} = 4\pi M_d(T_d) \kappa_\lambda B_\lambda(T_d), \quad (26)$$

where κ_λ and B_λ have been defined before (equation 10). We adopt this formula to estimate the mass contributed by dust in thermal equilibrium in stellar birth clouds (with temperature $T_d = T_W^{\text{BC}}$) and in the ambient ISM (with temperatures $T_d = T_W^{\text{ISM}}$ and $T_d = T_c^{\text{ISM}}$) in our model. We adopt as before a dust emissivity index $\beta = 1.5$ for warm dust and $\beta = 2$ for cold dust and normalise κ_λ at 850 μ m assuming $\kappa_{850\mu\text{m}} = 0.77 \text{ g}^{-1} \text{ cm}^2$ (Dunne et al. 2000). Using equations (10), (13), (15) and (26), we compute the mass contributed by warm dust in stellar birth clouds and in the ambient ISM as

$$M_W^{\text{BC}} = \xi_W^{\text{BC}} (1 - f_\mu) L_d^{\text{tot}} \left[4\pi \int_0^\infty d\lambda \kappa_\lambda B_\lambda(T_W^{\text{BC}}) \right]^{-1} \quad (27)$$

be constrained in galaxies with observed infrared spectral energy distributions.

and

$$M_W^{\text{ISM}} = \xi_W^{\text{ISM}} f_\mu L_d^{\text{tot}} \left[4\pi \int_0^\infty d\lambda \kappa_\lambda B_\lambda(T_W^{\text{ISM}}) \right]^{-1}, \quad (28)$$

and that contributed by cold dust in the ambient ISM as

$$M_C^{\text{ISM}} = \xi_C^{\text{ISM}} f_\mu L_d^{\text{tot}} \left[4\pi \int_0^\infty d\lambda \kappa_\lambda B_\lambda(T_C^{\text{ISM}}) \right]^{-1}. \quad (29)$$

To include the contribution by stochastically heated dust grains (not in thermal equilibrium; see Section 2.2.1), we adopt a standard Mathis et al. (1977) distribution of grain sizes $N(a) \propto a^{-3.5}$ over the range $0.005 \mu\text{m} \leq a \leq 0.25 \mu\text{m}$. We assume that the stochastically heated dust grains are very small ($a \leq 0.01 \mu\text{m}$) and have mass densities typical of graphite, $\rho \approx 2.26 \text{ g cm}^{-3}$, while bigger grains in thermal equilibrium have mass densities typical of silicates, $\rho \approx 3.30 \text{ g cm}^{-3}$ (Draine & Lee 1984). For these assumptions, the mass contributed by grains of all sizes is about 5 per cent larger than that contributed by big grains alone ($a > 0.01 \mu\text{m}$). The contribution by PAHs to the overall dust mass is also very small, of the order of a few per cent (Draine et al. 2007). We therefore estimate the total dust mass of a galaxy as

$$M_d \approx 1.1 (M_W^{\text{BC}} + M_W^{\text{ISM}} + M_C^{\text{ISM}}), \quad (30)$$

where M_W^{BC} , M_W^{ISM} and M_C^{ISM} are given by equations (27), (28) and (29).

2.3 Combined ultraviolet, optical and infrared spectral energy distributions

A main feature of our model is the consistent modelling of ultraviolet, optical and infrared spectral energy distributions of galaxies. This is achieved by first computing the total energy absorbed by dust in stellar birth clouds and in the ambient ISM, L_d^{BC} and L_d^{ISM} (Section 2.1), and then re-distributing it at infrared wavelengths (Section 2.2). The main assumptions are the conservation of the energy absorbed and reradiated by dust, and that the dust in the ISM of galaxies is heated only by starlight (in particular, we ignore the possible influence of an active galactic nucleus). Different combinations of star formation histories, metallicities and dust contents can lead to the same absorbed energies L_d^{BC} and L_d^{ISM} in a model galaxy. Furthermore, these energies can be distributed in wavelength using different combinations of dust parameters in the stellar birth clouds ($\xi_{\text{PAH}}^{\text{BC}}$, $\xi_{\text{MIR}}^{\text{BC}}$, ξ_W^{BC} and T_W^{BC}) and the ambient ISM (ξ_C^{ISM} and T_C^{ISM}). In our model, therefore, a wide range of ultraviolet and optical spectral energy distributions can be associated to a wide range of infrared spectral energy distributions, at fixed L_d^{BC} and L_d^{ISM} (or equivalently, at fixed f_μ and L_d^{tot} ; see equations 5 and 8). In Section 3 below, we show how combined observations at ultraviolet, optical and infrared wavelengths can be used to uniquely constrain the star formation histories and dust properties of galaxies using this model.

To illustrate the combination of ultraviolet, optical and infrared spectral energy distributions with our model, we compute examples of attenuated stellar population spectra consistent with the f_μ parameters of the cold, standard and hot infrared models of Table 1 (Section 2.2.2). For simplicity,

we assume solar metallicity and select models with exponentially declining star formation rates

$$\psi(t) \propto \exp(-\gamma t), \quad (31)$$

where γ is the star formation timescale parameter. We choose models with $\gamma = 0, 0.07$ and 0.25 Gyr^{-1} at the ages $t = 1.4, 10$ and 10 Gyr , respectively, to represent a starburst, a normal star-forming and a quiescent star-forming galaxy (e.g. Kauffmann & Charlot 1998). For the attenuation of starlight by dust (equations 3 and 4), we adopt effective dust absorption optical depths $\hat{\tau}_V = 2.0, 1.5$ and 1.0 , for the starburst, normal star-forming and quiescent star-forming models, respectively. These values are consistent with the expectation that more actively star-forming galaxies are more obscured (e.g. Wang & Heckman 1996; Hopkins et al. 2001; Sullivan et al. 2001). We adopt fractions $\mu = 0.1, 0.3$ and 0.5 of $\hat{\tau}_V$ arising from dust in the ambient ISM. The resulting model galaxies have $f_\mu \approx 0.2, 0.6$ and 0.75 , respectively, consistent with the parameters of the hot, standard and cold infrared models of Table 1.

In Fig. 5, we show the combined spectral energy distributions of the starburst + hot infrared, normal star-forming + standard infrared, and quiescent star-forming + cold infrared models, after scaling in each case the infrared luminosity to the total luminosity L_d^{tot} absorbed by dust. As we shall see in the next section, the ability to compute such combined ultraviolet, optical and infrared spectral energy distributions for wide ranges of physical parameters of galaxies has important implications for statistical estimates of star formation histories and dust properties.

3 CONSTRAINTS ON PHYSICAL PARAMETERS FROM MULTI-WAVELENGTH GALAXY OBSERVATIONS

In this section, we show how the simple model described in Section 2 can be used to extract star formation histories and dust properties from ultraviolet, optical and infrared observations of galaxies. In Section 3.1, we first describe our methodology to derive statistical constraints on galaxy physical parameters from multi-wavelength observations. Then, in Section 3.2, we use this methodology to constrain the physical parameters of star-forming galaxies in the SINGS sample. We compare our results to those that would be obtained using previous models in Section 3.3. Finally, we discuss possible sources of systematic errors associated with our approach in Section 3.4 and summarize the applicability of this model in Section 3.5.

3.1 Methodology

The model of Section 2 allows one to compute the ultraviolet, optical and infrared emission from galaxies. This model contains a minimum number of adjustable parameters required to account for the observed relations between various integrated spectral properties of galaxies: age, star formation history, stellar metallicity, two components for the attenuation by dust and four contributors to the infrared emission (PAHs, hot mid-infrared continuum, warm and cold dust in thermal equilibrium). The large number of observable

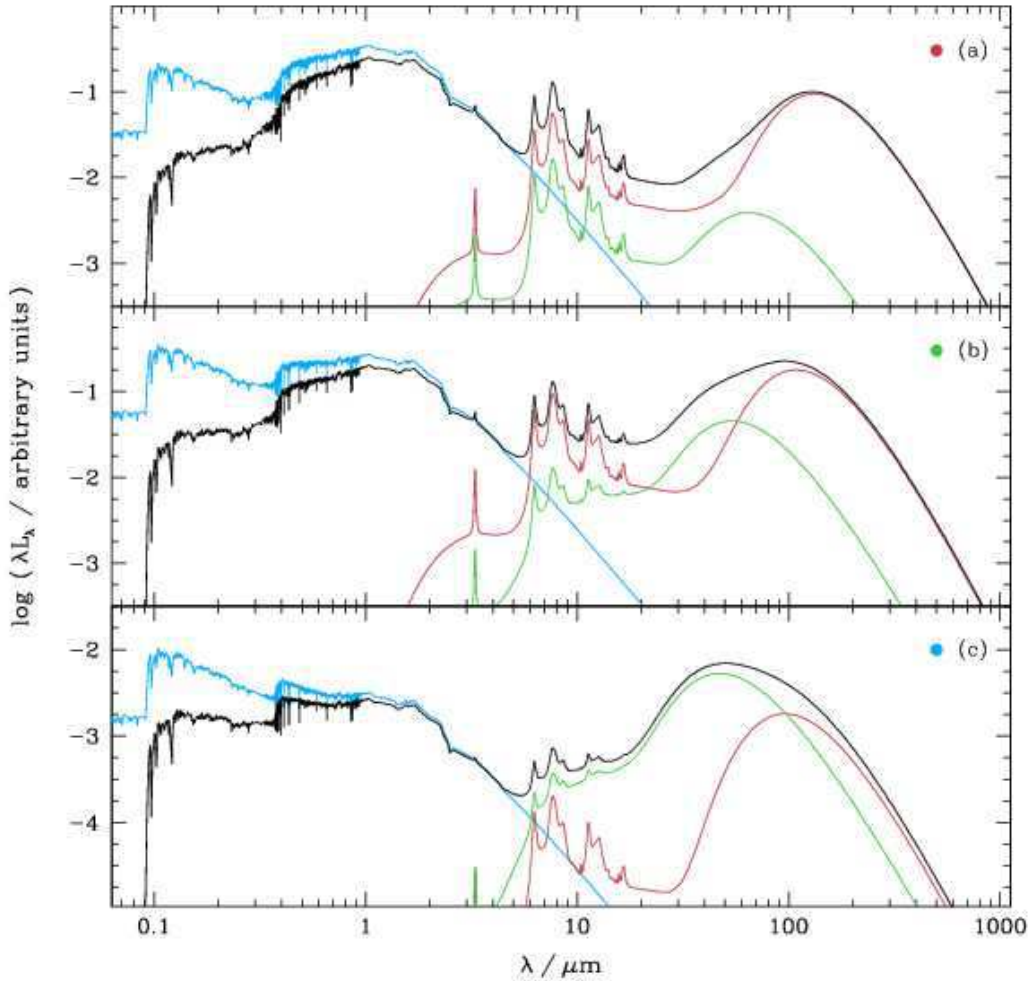


Figure 5. Examples of spectral energy distributions obtained by combining the infrared models of Table 1 with attenuated stellar population spectra corresponding to the same contributions by dust in stellar birth clouds ($1 - f_{\mu}$) and in the ambient ISM (f_{μ}) to the total energy $L_{\text{d}}^{\text{tot}}$ absorbed and reradiated by dust (Section 2.3). (a) Quiescent star-forming galaxy spectrum combined with the ‘cold’ infrared model of Table 1; (b) normal star-forming galaxy spectrum combined with the ‘standard’ infrared model of Table 1; (c) starburst galaxy spectrum combined with the ‘hot’ infrared model of Table 1 (see text for details about the parameters of the stellar population models). Each panel shows the unattenuated stellar spectrum (blue line), the emission by dust in stellar birth clouds (green line), the emission by dust in the ambient ISM (red line) and the total emission from the galaxy, corresponding to the sum of the attenuated stellar spectrum and the total infrared emission (black line).

quantities to which the model can be compared insures that these different adjustable parameters can be constrained in a meaningful way (see below). A usual limitation of this type of study is that several different combinations of physical parameters can lead to similar spectral energy distributions of galaxies. For example, age, metallicity and dust attenuation have similar effects on the ultraviolet and optical spectra of galaxies. An efficient way to derive statistical constraints on the various parameters in these conditions is to consider a wide library of models encompassing all plausible parameter combinations. Given an observed galaxy, we can build the likelihood distribution of any physical parameter by evaluating how well each model in the library can account for the observed properties of the galaxy. This Bayesian approach is similar to that used, for example, by Kauffmann et al.

(2003) to interpret the optical spectra of SDSS galaxies. The underlying assumption is that the library of models is the distribution from which the data were randomly drawn. Thus, the prior distribution of models must be such that the entire observational space is reasonably well sampled, and that no a priori implausible corner of parameter space accounts for a large fraction of the models.

3.1.1 Model library

We build a comprehensive library of models by generating separately a random library of stellar population models, for wide ranges of star formation histories, metallicities and dust contents, and a random library of infrared spectra, for wide ranges of dust temperatures and fractional contribu-

tions by the different dust components to the total infrared luminosity. We then combine these libraries following the procedure outline in Section 2.3.

For simplicity, we follow Kauffmann et al. (2003) and parametrise each star formation history in the stellar population library in terms of two components: an underlying continuous model, characterised by an age t_g and a star formation time-scale parameter γ (equation 31), and random bursts superimposed on this continuous model. We take t_g to be uniformly distributed over the interval from 0.1 and 13.5 Gyr. To avoid oversampling galaxies with negligible current star formation, we distribute γ using the probability density function $p(\gamma) = 1 - \tanh(8\gamma - 6)$, which is approximately uniform over the interval from 0 to 0.6 Gyr^{-1} and drops exponentially to zero around $\gamma = 1 \text{ Gyr}^{-1}$. Random bursts occur with equal probability at all times until t_g . We set the probability so that 50 per cent of the galaxies in the library have experienced a burst in the past 2 Gyr. We parametrise the amplitude of each burst as $A = M_{\text{burst}}/M_{\text{cont}}$, where M_{burst} is the mass of stars formed in the burst and M_{cont} is the total mass of stars formed by the continuous model over the time t_g . This ratio is distributed logarithmically between 0.03 and 4.0. During a burst, stars form at a constant rate over the time t_{burst} , which we distribute uniformly between 3×10^7 and 3×10^8 yr. We distribute the models uniformly in metallicity between 0.02 and 2 times solar.

We sample attenuation by dust in the library by randomly drawing the total effective V-band absorption optical depth, $\hat{\tau}_V$, and the fraction of this contributed by dust in the ambient ISM, μ (equations 3 and 4). We distribute $\hat{\tau}_V$ according to the probability density function $p(\hat{\tau}_V) = 1 - \tanh(1.5\hat{\tau}_V - 6.7)$, which is approximately uniform over the interval from 0 to 4 and drops exponentially to zero around $\hat{\tau}_V = 6$. For μ , we adopt the same probability density function as for γ above, i.e. $p(\mu) = 1 - \tanh(8\mu - 6)$. We note that these priors for attenuation encompass the dust properties of SDSS galaxies, for which $\hat{\tau}_V$ and μ peak around 1.0 and 0.3, respectively, with broad scatter (Brinchmann et al. 2004; Kong et al. 2004). Our final stellar population library consists of 50,000 different models.

In parallel, we generate a random library of infrared spectra as follows. We take the fraction f_μ of the total infrared luminosity contributed by dust in the ambient ISM to be uniformly distributed over the interval from 0 to 1. We adopt a similar distribution for the fractional contribution by warm dust in thermal equilibrium to the infrared luminosity of stellar birth clouds, ξ_W^{BC} . For each random drawing of ξ_W^{BC} , we successively draw the contributions by the other dust components to the infrared luminosity of stellar birth clouds (i.e., hot mid-infrared continuum and PAHs) to satisfy the condition in equation (14): we draw $\xi_{\text{MIR}}^{\text{BC}}$ from a uniform distribution between 0 and $1 - \xi_W^{\text{BC}}$, and we set $\xi_{\text{PAH}}^{\text{BC}} = 1 - \xi_W^{\text{BC}} - \xi_{\text{MIR}}^{\text{BC}}$. While this procedure does not exclude values of $\xi_{\text{MIR}}^{\text{BC}}$ and $\xi_{\text{PAH}}^{\text{BC}}$ close to unity, it does favour small values of these parameters, and hence, it avoids oversampling physically implausible models. We take the equilibrium temperature T_W^{BC} of warm dust in the stellar birth clouds to be uniformly distributed between 30 and 60 K, and that T_C^{ISM} of cold dust in the ambient ISM to be uniformly distributed between 15 and 25 K. We draw the fractional contribution ξ_C^{ISM} by cold dust in thermal equilibrium to

the infrared luminosity of the ambient ISM from a uniform distribution between 0.5 and 1 (this also defines the contributions $\xi_{\text{PAH}}^{\text{ISM}}$, $\xi_{\text{MIR}}^{\text{ISM}}$ and ξ_W^{ISM} by PAHs, the hot mid-infrared continuum and warm dust to the infrared luminosity of the ambient ISM, as described in Section 2.2.1). Our final library of infrared spectra consists of 50,000 different models.

We combine the library of stellar population models and that of infrared spectra by associating together models with similar f_μ , which we scale according to the total infrared luminosity L_d^{tot} , as outlined in Section 2.3. In practice, we associate each model in the stellar population library to all the models in the infrared spectral library that have similar f_μ to within some error interval δf_μ .⁵ That is, we associate each stellar population spectrum, characterised by f_μ^{SFH} , to all the infrared spectra characterised by f_μ^{IR} , such that $f_\mu^{\text{IR}} = f_\mu^{\text{SFH}} \pm \delta f_\mu$. Each spectral combination satisfying this condition is included in the final model library and is assigned a value $f_\mu = (f_\mu^{\text{SFH}} + f_\mu^{\text{IR}})/2$. We adopt $\delta f_\mu = 0.15$, which allows good reproductions of combined ultraviolet, optical and infrared observations of galaxies (Section 3.2).

Our final library of combined ultraviolet, optical and infrared spectral energy distributions consists of about 661 million models. It is important to note that such a large number of models is required to properly sample the multi-dimensional observational space.

3.1.2 Statistical constraints on physical parameters

We now investigate the accuracy to which the model library described in the previous section can help us constrain the star formation histories and dust properties of galaxies for which multi-wavelength observations are available. To assess this, we evaluate how well we can recover the parameters of a random set of models with known properties, based on spectral fits. We consider the following observable quantities: the *GALEX* far-ultraviolet (*FUV*, 1520 Å) and near-ultraviolet (*NUV*, 2310 Å) luminosities; the optical *UBV* luminosities; the 2MASS near-infrared *JHKs* (1.25, 1.65 and 2.17 μm) luminosities; the *Spitzer*/IRAC 3.6, 4.5, 5.8 and 8.0 μm luminosities; the *ISO*/ISOCAM 6.75 and 15 μm luminosities; the *IRAS* 12, 25, 60 and 100 μm luminosities; the *Spitzer*/MIPS (Rieke et al. 2004) 24, 70 and 160 μm luminosities; and the SCUBA (Holland et al. 1999) 850 μm luminosity. We also include the hydrogen H α and H β recombination-line luminosities.

We compute these observable quantities from the spectra of all 661 million models in the library and randomly select a subset of 100 models. To mimic observational conditions, we perturb the luminosities of this subset of models assuming a fixed uncertainty of 10 per cent. We then perform spectral fits to recover the likelihood distributions of the physical parameters of these ‘mock galaxies’ as follows. We first compare the luminosities of each mock galaxy in the sample to the luminosities of every model j in the library to measure the χ^2 goodness-of-fit of that model (e.g., Bevington & Robinson 2003)

⁵ This allows us to include the uncertainties that could arise, for example, from orientation effects, in the connection between the stellar and dust emission.

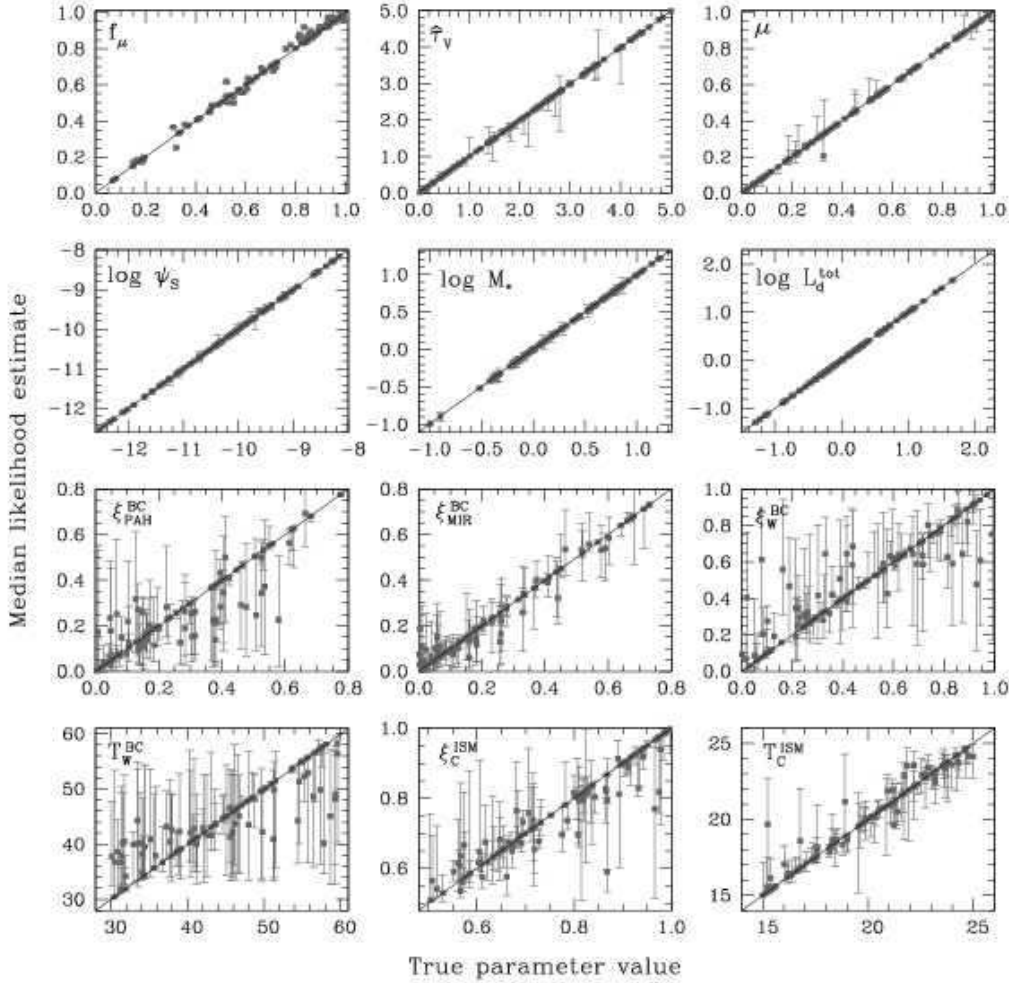


Figure 6. Median-likelihood estimates of 12 parameters (indicated in the upper left corner of each panel) recovered from the spectral fits of 100 mock galaxies, compared to the true values of these parameters (see Section 3.1.2). The error bars indicate the 16–84 percentile ranges in the recovered probability distributions of the parameters. These results were obtained by fitting simulated *GALEX* (*FUV* and *NUV*), optical (*UBV*), 2MASS (*JHKs*), *Spitzer*/IRAC (3.6, 4.5, 5.8 and 8.0 μm), *ISO*/ISOCAM (6.75 and 15 μm), *IRAS* (12, 25, 60, 100 μm), *Spitzer*/MIPS (24, 70, and 160 μm), SCUBA (850 μm), and $\text{H}\alpha$ and $\text{H}\beta$ luminosities.

$$\chi_j^2 = \sum_i \left(\frac{L_{\nu}^i - w_j \times L_{\nu,j}^i}{\sigma_i} \right)^2, \quad (32)$$

where L_{ν}^i and $L_{\nu,j}^i$ are the luminosities in the i^{th} band of the mock galaxy and the j^{th} model, respectively, σ_i is the (10 percent) uncertainty in L_{ν}^i , and

$$w_j = \left(\sum_i \frac{L_{\nu}^i L_{\nu,j}^i}{\sigma_i^2} \right) \left[\sum_i \left(\frac{L_{\nu,j}^i}{\sigma_i} \right)^2 \right]^{-1} \quad (33)$$

is the model scaling factor that minimizes χ_j^2 . Then, we build the probability density function of any physical parameter of the mock galaxy by weighting the value of that parameter in the j^{th} model by the probability $\exp(-\chi_j^2/2)$. We take our ‘best estimate’ of the parameter to be the median of the resulting probability density function and the associated confidence interval to be the 16–84 percentile range

(this would be equivalent to the $\pm 1\sigma$ range in the case of a Gaussian distribution).

In Fig. 6, we compare the median-likelihood estimates to the true values of 12 parameters recovered in this way for the 100 mock galaxies in our sample. These parameters are: the fraction of total infrared luminosity contributed by dust in the ambient ISM, f_{μ} ; the total effective *V*-band absorption optical depth of the dust, $\hat{\tau}_V$; the fraction of this contributed by dust in the ambient ISM, μ ; the specific star formation rate, ψ_S , defined as the ratio

$$\psi_S(t) = \frac{\int_{t-t_8}^t dt' \psi(t')}{t_8 M_*} \quad (34)$$

of the star formation rate averaged over the past $t_8 = 10^8 \text{ yr}$ to the current stellar mass M_* of the galaxy; the stellar mass, M_* (this accounts for the mass returned to the ISM by evolved stars); the total infrared luminosity, L_d^{tot} ; the fractional contributions by PAHs, the hot mid-infrared con-

tinuum and warm dust in thermal equilibrium to the infrared luminosity of stellar birth clouds, $\xi_{\text{PAH}}^{\text{BC}}$, $\xi_{\text{MIR}}^{\text{BC}}$ and $\xi_{\text{W}}^{\text{BC}}$; the equilibrium temperature of warm grains in stellar birth clouds, T_{W}^{BC} ; the contribution by cold dust to the total infrared luminosity of the ambient ISM, $\xi_{\text{C}}^{\text{ISM}}$, and the equilibrium temperature of this dust, $T_{\text{C}}^{\text{ISM}}$. Most of these parameters are recovered remarkably well by our model. In particular, f_{μ} , $\hat{\tau}_{\text{V}}$, μ , ψ_{S} , M_{\star} , $L_{\text{d}}^{\text{tot}}$, $\xi_{\text{MIR}}^{\text{BC}}$, $\xi_{\text{C}}^{\text{ISM}}$ and $T_{\text{C}}^{\text{ISM}}$ are recovered to very high accuracy. The most uncertain parameters are $\xi_{\text{PAH}}^{\text{BC}}$, $\xi_{\text{W}}^{\text{BC}}$ and T_{W}^{BC} , for which the typical confidence intervals reach almost 0.14, 0.18 and 11 K, respectively. We conclude that our model is a valuable tool for deriving statistical constraints on the star formation histories and dust properties of galaxies for which multi-wavelength (ultraviolet, optical and infrared) observations are available.

3.2 Application to an observational sample

3.2.1 The sample

Here, we exploit our model to interpret a wide range of ultraviolet, optical and infrared observations of a sample of well-studied nearby galaxies: the Spitzer Infrared Nearby Galaxy Survey (SINGS; Kennicutt et al. 2003). This sample contains 75 galaxies at a median distance of 9.5 Mpc (we adopt a Hubble constant $H_0 = 70 \text{ km s}^{-1} \text{ Mpc}^{-1}$). The galaxies span wide ranges in morphology (from E-S0 to Im-I0) and star formation activity (from quiescent to starburst). Some galaxies include low-luminosity active galactic nuclei (AGNs).⁶ We note that this sample extends out to lower total infrared luminosities than the Elbaz et al. (2002) sample used to calibrate the infrared properties of our model in Section 2.2.2 ($L_{\text{d}}^{\text{tot}} \lesssim 10^{11} L_{\odot}$ instead of $L_{\text{d}}^{\text{tot}} \lesssim 10^{12} L_{\odot}$), but it includes observations across a much wider range of wavelengths.

Observations at ultraviolet, optical and infrared wavelengths are available for most galaxies in this sample. *GALEX* ultraviolet (*NUV* and *FUV*) observations are available for 70 galaxies (Dale et al. 2007). In the optical, we adopt *UBV* fluxes from the RC3 for 65 galaxies (de Vaucouleurs et al. 1991).⁷ Near-infrared *JHKs* fluxes are available for all galaxies from the 2MASS Large Galaxy Atlas (Jarrett et al. 2003). In the mid- and far-infrared, we use the *Spitzer* observations published by Dale et al. (2007). This includes IRAC photometry at 3.6, 4.5, 5.8 and 8.0 μm and MIPS photometry at 24, 70 and 160 μm . *ISO*, *IRAS* and SCUBA 850 μm observations are also available for 13, 65 and 22 SINGS galaxies, respectively. These observations are typically of lower quality than *Spitzer* data, with photometric uncertainties around 20 per cent for *ISO* and *IRAS* and 30 per cent for SCUBA. More detail about the photometry of SINGS galaxies can be found in Dale et al. (2005, 2007).

⁶ The low-luminosity AGNs should have a negligible impact on the integrated broad-band fluxes of the galaxies. We distinguish galaxies hosting low-luminosity AGNs from normal star-forming galaxies in the spectral analyses presented later in this paper.

⁷ We choose not to use the optical *BVRI* fluxes tabulated by Dale et al. (2007), because of calibration problems in the optical photometry of the SINGS Fifth Enhanced Data Release (D. Dale & A. Gil de Paz, priv. comm.)

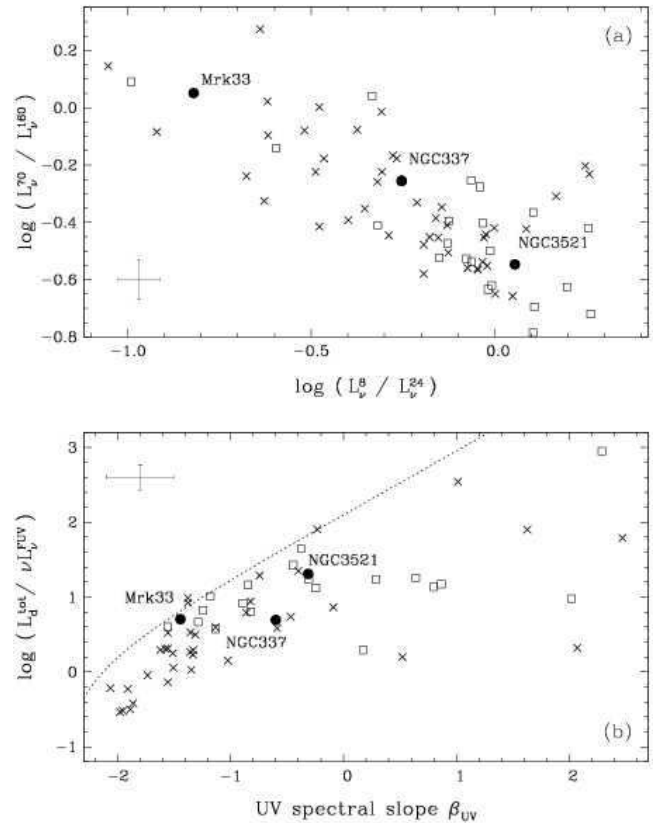


Figure 7. Selected properties of the SINGS galaxy sample discussed in Section 3.2. (a) Ratio of 70- μm to 160- μm luminosity plotted against ratio of 8- μm to 24- μm luminosity. (b) Ratio of total-infrared to ultraviolet luminosity as a function of ultraviolet spectral slope (the IRX–UV diagram). The dotted line in this diagram shows a fit by Kong et al. (2004) to the relation followed by starburst galaxies (Meurer et al. 1999). In both panels, crosses refer to galaxies with no AGN activity according to Kennicutt et al. (2003), while open squares refer to galaxies hosting low-luminosity AGNs (LINER and Seyfert). Filled circles indicate three galaxies selected along the $L_{\nu}^{70}/L_{\nu}^{160}$ versus L_{ν}^8/L_{ν}^{24} relation, for which a wide set of observations are available (Section 3.2.2). Typical measurement errors are indicated in each diagram.

It is important to note that these multi-wavelength observations can be combined in a meaningful way, since the fluxes all pertain to the total emission from a galaxy. For example, the *GALEX* (*FUV* and *NUV*), RC3 (*UBV*) and 2MASS (*JHKs*) fluxes were obtained by integrating extrapolated surface brightness profiles to include the entire emission from a galaxy (see de Vaucouleurs et al. 1991; Jarrett et al. 2003; Gil de Paz et al. 2006). Also, the infrared *Spitzer* IRAC and MIPS fluxes include extended-source aperture corrections (amounting typically to 10 per cent; see Dale et al. 2005, 2007). Following Draine et al. (2007), we exclude 9 galaxies with bad IRAC and MIPS detections (because of contamination by external sources; very low surface brightness compared to foreground cirrus emission; and saturation issues): NGC 584, NGC 3034, NGC 1404, NGC 4552, M81 DwarfA, M81 DwarfB, DDO 154, DDO 165 and Holmberg IX. For 19 galaxies, we

include $H\alpha$ and $H\beta$ emission-line fluxes (corrected for contamination by stellar absorption) from the integrated spectroscopy of Moustakas & Kennicutt (2006). Our final sample includes 66 galaxies, of which 61 have *GALEX* measurements. As before, for the purpose of comparisons with models, we neglect possible anisotropies and equate flux ratios at all wavelengths to the corresponding luminosity ratios.

We illustrate the ultraviolet and infrared properties of the SINGS galaxies in Fig. 7. Fig. 7a shows the MIPS L_ν^{70}/L_ν^{160} luminosity ratio plotted against the IRAC+MIPS L_ν^8/L_ν^{24} luminosity ratio. SINGS galaxies in this diagram follow a sequence very similar to that followed by the galaxies of the Elbaz et al. (2002) sample of Section 2.2 in the analogous *IRAS* L_ν^{60}/L_ν^{100} versus L_ν^{12}/L_ν^{25} diagram (Fig. 3). In Fig. 7b, we plot ratio of total-infrared to ultraviolet luminosity $L_d^{\text{tot}}/L_{\text{FUV}}$ as a function of ultraviolet spectral slope β_{UV} (the ‘IRX-UV diagram’). We used equation (4) of Dale & Helou (2002) to estimate L_d^{tot} from the MIPS observations at 24, 70 and 160 μm , and equation (1) of Kong et al. (2004) to compute β_{UV} from the *GALEX* *FUV* and *NUV* luminosities. Previous studies have shown that starburst galaxies follow a tight sequence in this diagram (indicated by the dotted line in Fig. 7b), while more quiescent star-forming galaxies tend to exhibit redder ultraviolet spectra (i.e. larger β_{UV}) than starburst galaxies at fixed $L_d^{\text{tot}}/L_{\text{FUV}}$ (Meurer et al. 1999; Bell 2002; Kong et al. 2004). Fig. 7 confirms that the SINGS galaxies are representative of the ultraviolet and infrared properties of nearby galaxies.

3.2.2 Example of constraints on physical parameters

We now use the methodology outlined in Section 3.1 to constrain the star formation histories and dust properties of the SINGS galaxies. We first assess how well our model can reproduce the observed multi-wavelength observations of these galaxies. For each observed galaxy, we select the model of the library presented in Section 3.1 that minimizes χ_j^2 (equation 32), as computed by including as many luminosities as available in the following bands: *GALEX* (*FUV* and *NUV*), optical (*UBV*), 2MASS (*JHKs*), *Spitzer*/IRAC (3.6, 4.5, 5.8 and 8.0 μm), *ISO*/ISOCAM (6.75 and 15 μm), *IRAS* (12, 25, 60 and 100 μm), *Spitzer*/MIPS (24, 70 and 160 μm), SCUBA (850 μm) and $H\alpha$ and $H\beta$. Fig. 8 shows the resulting distribution of the difference between the observed luminosity L_ν^{obs} and the best-fit model luminosity L_ν^{mod} , in units of the observational error σ^{obs} , for the 66 galaxies in the sample (plain histograms). Each panel shows the result for a different photometric band. For reference, the shaded histograms show the results obtained when excluding the 22 galaxies identified as hosts of low-luminosity AGNs by Kennicutt et al. (2003).

Fig. 8 shows that our model can reproduce simultaneously the ultraviolet, optical and near-, mid- and far-infrared observations of all but a few SINGS galaxies to within the observational errors. This is remarkable, considering the relative simplicity of the model. We find that the galaxies the least well fitted at ultraviolet and optical wavelengths tend to be low-metallicity dwarf galaxies, such as the blue compact dwarf galaxy NGC 2915 (e.g. Lee et al. 2003) and the diffuse dwarf irregular galaxy Holmberg II (e.g. Hoessel et al. 1998). The difficulty in reproducing these ob-

servations may arise either from a limitation of the spectral synthesis code, or of the simple dust prescription, or from an underestimate of observational errors. The three galaxies for which the models significantly underestimate the 3.6 μm emission in Fig. 8 are also low-metallicity dwarf galaxies (NGC4236, IC4710 and NGC6822). For these galaxies, our simple scaling of the near-infrared continuum strength around 4 μm with the flux density of the 7.7 μm PAH feature may not be appropriate (see Section 2.2.1). Fig. 8 further shows that the galaxies with 8 μm mid-infrared luminosities least well reproduced by the model tend to be hosts of low-luminosity AGNs. In these galaxies, the contribution to the infrared emission by dust heated by the AGN may be significant. Despite these few outliers, we conclude from Fig. 8 that our model is adequate to investigate the constraints set on the physical properties of SINGS galaxies by their ultraviolet, optical and infrared spectral energy distributions.

To investigate the implications of these fits for the determination of physical parameters, we focus on three galaxies spanning different dust properties along the L_ν^{70}/L_ν^{160} versus L_ν^8/L_ν^{24} colour-colour relation in Fig. 7a, for which a wide set of observations are available: NGC 3521, a spiral (SABbc) galaxy at a distance of 9 Mpc; NGC 337, a spiral (SBd) galaxy at a distance of 24.7 Mpc; and Mrk 33, a dwarf irregular (Im) starburst galaxy at a distance of 21.7 Mpc. For all three galaxies, observations from *GALEX* (*FUV* and *NUV*), 2MASS (*JHKs*), *Spitzer* (IRAC and MIPS), *IRAS* and SCUBA are available, along with integrated $H\alpha$ and $H\beta$ spectroscopy from Moustakas & Kennicutt (2006). For NGC 3521 and NGC 337, additional constraints are available from RC3 (*UBV*) and *ISO* (ISOCAM 6.75 and 15 μm) photometry.

Fig. 9 shows the models (in black) providing the best fits to the observed ultraviolet, optical, $H\alpha$ and $H\beta$, and infrared spectral energy distributions of these three galaxies (in red). The quality of the fits is remarkable, as quantified by the residuals shown at the bottom of each spectrum. We note that, according to the best-fit models, the sequence of increasing F_ν^{70}/F_ν^{160} and decreasing F_ν^8/F_ν^{24} colours from NGC 3521 to NGC 337 to Mrk 33, which reflects a drop in the relative intensity of PAHs and a blueshift of the peak infrared luminosity (i.e. a rise in the overall dust temperature), is associated to an increase in star formation activity. This is apparent from the relative strengthening of the unattenuated ultraviolet and optical spectrum (in blue) from NGC 3521 to NGC 337 to Mrk 33 in Fig. 9. We investigate this trend further in Section 3.2.3 below.

We can study in more detail the constraints set on the star formation histories and dust properties of the galaxies by looking at the probability distributions of the corresponding model parameters. In Figs. 10 and 11, we show the likelihood distributions of 14 quantities constrained by the observed spectral energy distributions of NGC 3521, NGC 337 and Mrk 33. These distributions were derived using the model library of Section 3.1.1, following the procedure outlined in Section 3.1.2. Fig. 10 shows the likelihood distributions of parameters pertaining to the star formation history and dust content: fraction of the total infrared luminosity contributed by dust in the ambient ISM (f_μ); fraction of the total effective *V*-band absorption optical depth of the dust contributed by the ambient ISM (μ); effective *V*-band absorption optical depth of the dust ($\hat{\tau}_V$); effective *V*-band

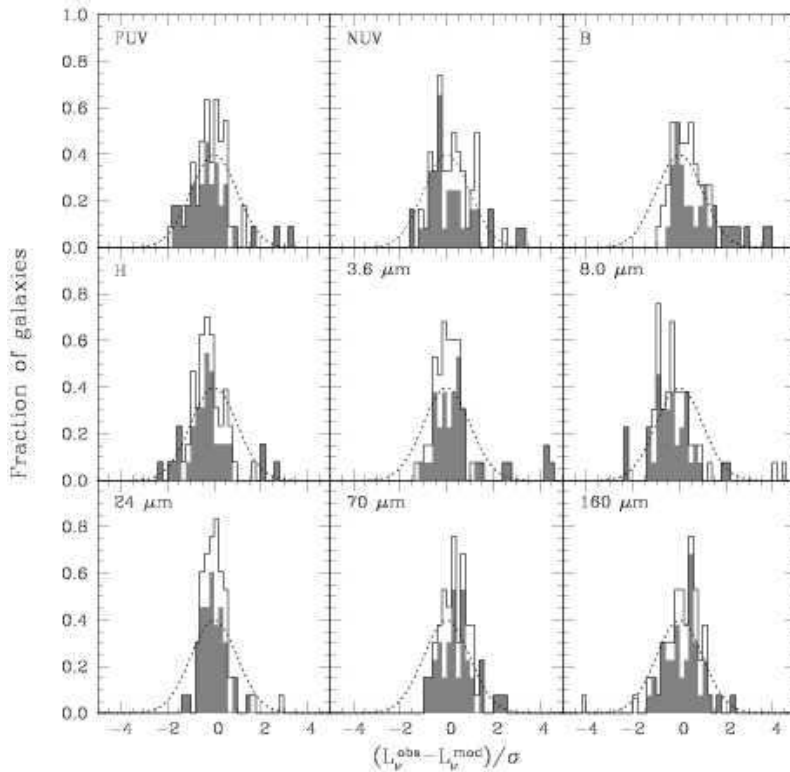


Figure 8. Distribution of the difference between observed luminosity L_{ν}^{obs} and best-fit model luminosity L_{ν}^{mod} , in units of the observational error σ^{obs} , for the 66 galaxies of the SINGS sample studied in Section 3.2. Each panel refers to a different photometric band (as indicated). The best-fit model for each galaxy was selected by fitting as many luminosities as available in the following bands: *GALEX* (*FUV* and *NUV*), optical (*UBV*), 2MASS (*JHKs*), *Spitzer*/*IRAC* (3.6, 4.5, 5.8 and 8.0 μm), *ISO*/*ISOCAM* (6.75 and 15 μm), *IRAS* (12, 25, 60 and 100 μm), *Spitzer*/*MIPS* (24, 70 and 160 μm), *SCUBA* (850 μm) and *H α* and *H β* . In each panel, the plain histogram shows the result for the full sample of 66 SINGS galaxies, while the shaded histogram shows the result for the subsample of 44 galaxies with no AGN activity according to Kennicutt et al. (2003). The dotted curve shows a Gaussian distribution with unit standard deviation, for reference.

absorption optical depth of the dust in the ambient ISM ($\mu\tau_V$); specific star formation rate (ψ_S ; equation 34); stellar mass (M_*); and dust mass (M_d ; equation 30). Fig. 11 shows the likelihood distributions of parameters pertaining to the dust emission: total infrared luminosity (L_d^{tot}); global contributions (i.e. including stellar birth clouds and the ambient ISM) by PAHs ($\xi_{\text{PAH}}^{\text{tot}}$), the hot mid-infrared continuum ($\xi_{\text{MIR}}^{\text{tot}}$) and warm dust in thermal equilibrium (ξ_W^{tot}) to the total infrared luminosity (equations 19, 20 and 21); equilibrium temperature of warm dust in stellar birth clouds (T_W^{BC}); contribution by cold dust in thermal equilibrium to the total infrared luminosity (ξ_C^{tot} , equation 22); and equilibrium temperature of cold dust in the ambient ISM (T_C^{ISM}).

The different histograms in Figs. 10 and 11 refer to different assumptions about the available set of observations. The grey shaded histograms show the results obtained when using all the observational measurements from Fig. 9. In this case, all the parameters are well constrained by the observed ultraviolet, optical and infrared spectral energy distributions of the galaxies, except for the equilibrium temperature T_W^{BC} of warm dust in stellar birth clouds in NGC 3521. This is not surprising, since the total infrared emission from this galaxy is largely dominated by dust in the ambient ISM (as can be appreciated, for example, from the analogous spectrum of

the quiescent star-forming galaxy of Fig. 5a). We find that, as anticipated from Fig. 9, the transition from NGC 3521 to NGC 337 to Mrk 33 corresponds to a combined rise in specific star formation rate (ψ_S) and dust temperature (T_W^{BC} and T_C^{ISM}), a larger contribution to the total infrared luminosity by warm dust (ξ_W^{tot}) relative to cold dust (ξ_C^{tot}), and by stellar birth clouds relative to the ambient ISM (f_μ), and a weakening of PAH features ($\xi_{\text{PAH}}^{\text{tot}}$). These results are consistent with the finding by Draine et al. (2007), on the basis of a more sophisticated physical dust model, that the intensity of the dust-heating starlight increases, and the fraction of dust mass contributed by PAHs decreases, from NGC 3521 to NGC 337 to Mrk 33. We emphasise the importance of finding tight constraints on all the adjustable model parameters in Figs. 10 and 11. This confirms that the problem is well defined and that our model can be used to derive meaningful constraints on the star formation histories and dust properties of galaxies from multi-wavelength observations.

In many situations, observations may not be available across the full range from ultraviolet to far-infrared wavelengths to constrain the physical parameters of galaxies. It is useful, therefore, to explore the constraints that can be derived on the physical parameters of Figs. 10 and 11 when

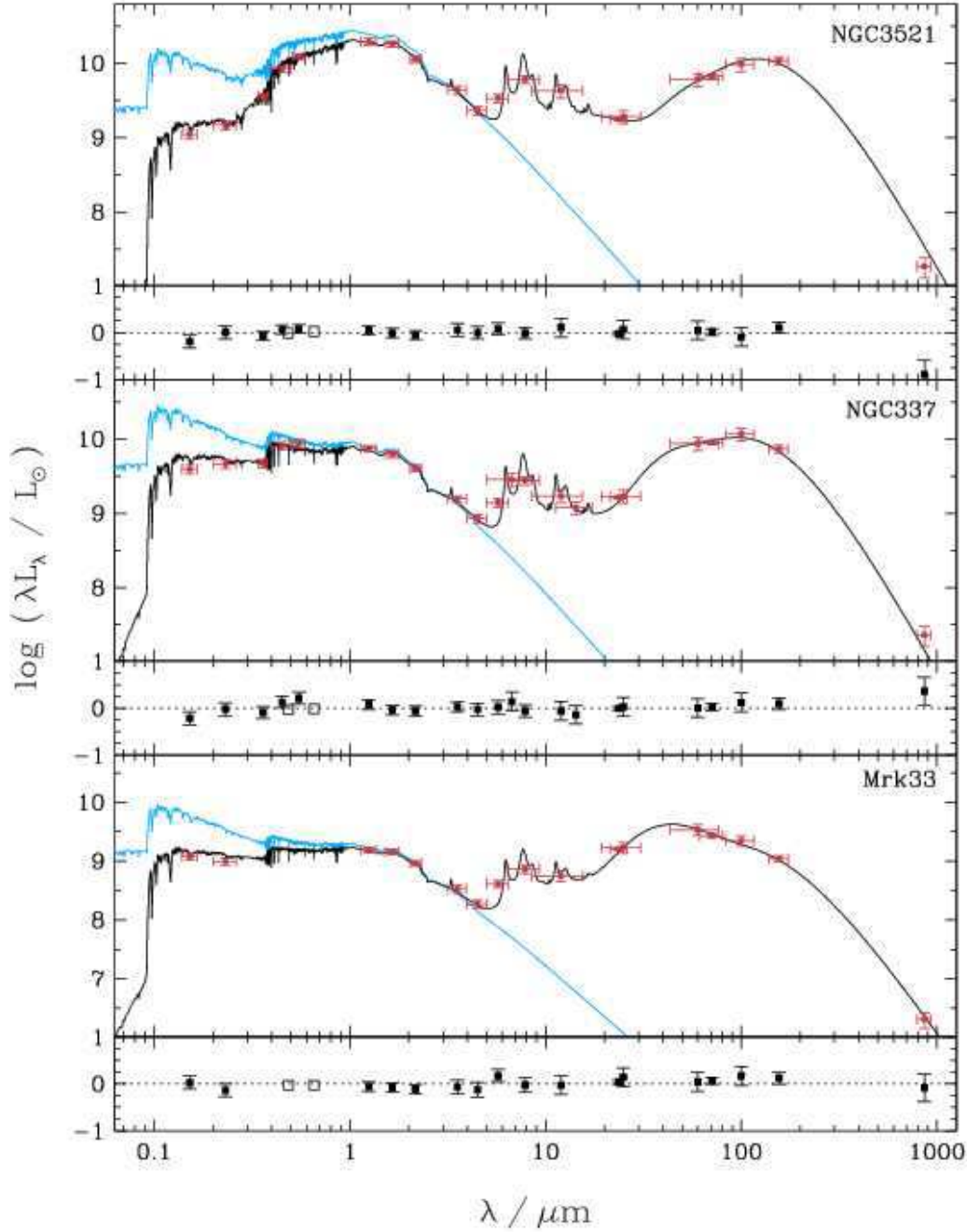


Figure 9. Best model fits (in black) to the observed spectral energy distributions (in red) of the three galaxies NGC 3521 (top panel), NGC 3521 (middle panel) and Mrk 33 (bottom panel) spanning the infrared colour-colour relation of Fig. 7a. In each panel, the blue line shows the unattenuated stellar population spectrum. For each observational point, the vertical error bar indicates the measurement error, while the horizontal error bar shows the effective width of the corresponding photometric bands. The residuals $(L_{\lambda}^{\text{obs}} - L_{\lambda}^{\text{mod}})/L_{\lambda}^{\text{obs}}$ are shown at the bottom of each panel. Filled squares refer to broad-band luminosities (*GALEX* *FUV* and *NUV*; RC3 *UBV*; 2MASS *JHKs*; *Spitzer* IRAC and MIPS; *ISO*, *IRAS* and SCUBA); open squares to the integrated $H\alpha$ and $H\beta$ luminosities.

reducing the set of available observations. We illustrate this by considering three potentially common situations:

(i) *Case I* (red histograms in Figs. 10 and 11): we relax the constraints on the $H\alpha$ and $H\beta$, *ISO*/ISOCAM (6.75

and 15 μm), *IRAS* (12, 25, 60 and 100 μm), *Spitzer*/MIPS 160 μm and SCUBA 850 μm luminosities. This leaves constraints from *GALEX* (*FUV* and *NUV*), RC3 (*UBV*), 2MASS (*JHKs*), *Spitzer*/IRAC (3.6, 4.5, 5.8 and 8.0 μm) and *Spitzer*/MIPS (24 and 70 μm).

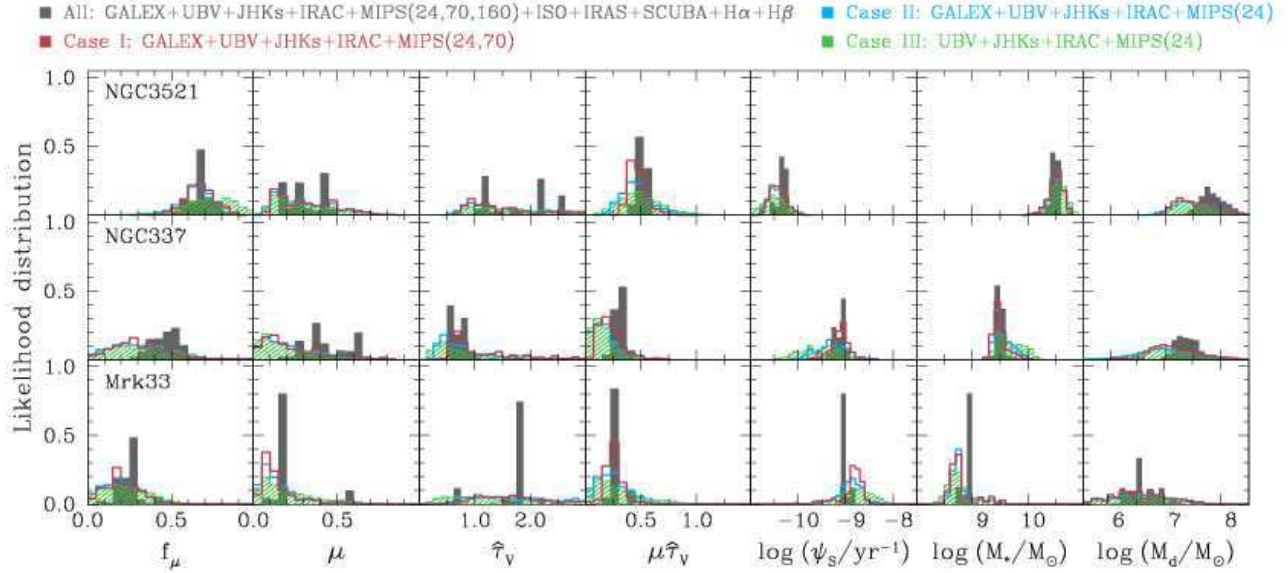


Figure 10. Likelihood distributions of physical quantities derived from fits to the observed ultraviolet, optical and infrared spectral energy distributions of NGC 3521 (top row), NGC 337 (middle row) and Mrk 33 (bottom row): fraction of the total infrared luminosity contributed by dust in the ambient ISM (f_μ); total effective V-band absorption optical depth of the dust ($\hat{\tau}_V$); fraction of the total V-band absorption optical depth of the dust contributed by the ambient ISM (μ); effective V-band absorption optical depth of the dust in the ambient ISM ($\mu\hat{\tau}_V$); specific star formation rate (ψ_S); stellar mass (M_*); and dust mass (M_d). The different histograms correspond to the different sets of observational constraints indicated at the top of the figure (see text of Section 3.2.2 for more detail).

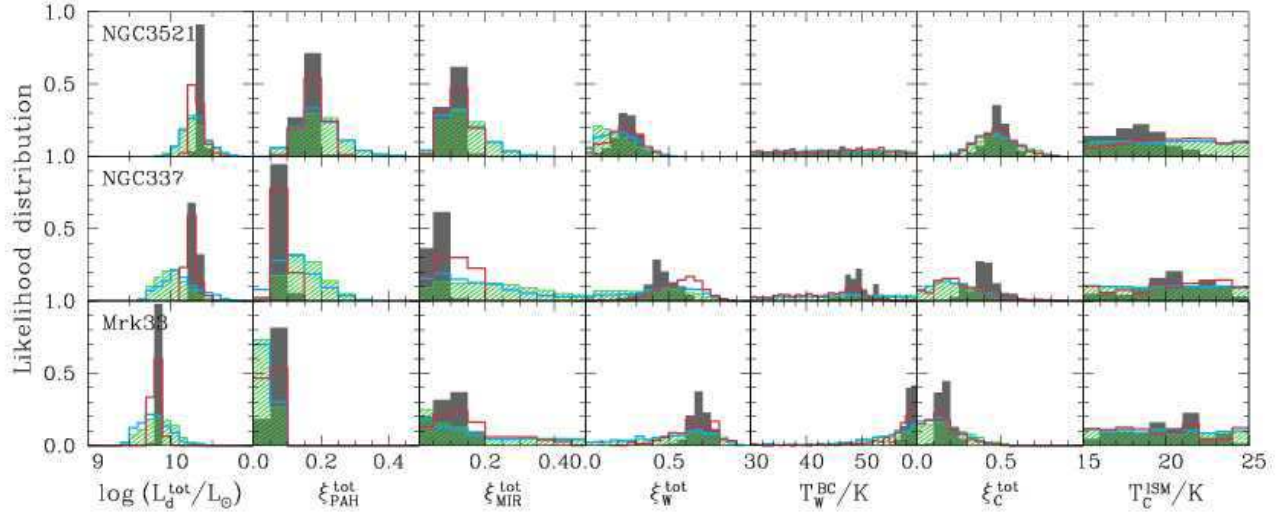


Figure 11. Likelihood distributions of physical quantities derived from fits to the observed ultraviolet, optical and infrared spectral energy distributions of NGC 3521 (top row), NGC 337 (middle row) and Mrk 33 (bottom row): total infrared luminosity of the dust (L_d^{tot}); global contributions (i.e. including stellar birth clouds and the ambient ISM) by PAHs ($\xi_{\text{PAH}}^{\text{tot}}$), the hot mid-infrared continuum ($\xi_{\text{MIR}}^{\text{tot}}$) and warm dust in thermal equilibrium ($\xi_{\text{W}}^{\text{tot}}$) to the total infrared luminosity; equilibrium temperature of warm dust in stellar birth clouds ($T_{\text{W}}^{\text{BC}}/\text{K}$); contribution by cold dust in thermal equilibrium to the total infrared luminosity ($\xi_{\text{C}}^{\text{tot}}$); and equilibrium temperature of cold dust in the ambient ISM ($T_{\text{C}}^{\text{ISM}}/\text{K}$). The different histograms correspond to the different sets of observational constraints indicated at the top of Fig. 10 (see text of Section 3.2.2 for more detail).

The most important effect of excluding the constraints on $L_{H\alpha}$ and $L_{H\beta}$ is to lose the determination of the total effective V -band absorption optical depth $\hat{\tau}_V$ in Fig. 10. This is because emission lines are the best tracers of dust in stellar birth clouds. In fact, the product $\mu\hat{\tau}_V$, i.e. the part of $\hat{\tau}_V$ arising from dust in the ambient ISM, remains reasonably well constrained by ultraviolet, optical and infrared photometry alone. In Fig. 11, the loss of far-infrared information redward of $70\ \mu\text{m}$ (*IRAS* $100\ \mu\text{m}$, *MIPS* $160\ \mu\text{m}$ and *SCUBA* $850\ \mu\text{m}$) has the most dramatic effect on determinations of the contribution by cold dust to the total infrared luminosity (ξ_C^{tot}) and on the equilibrium temperature of both cold (T_C^{ISM}) and warm (T_W^{BC}) dust. The *IRAC* data at wavelengths 3.6 , 4.5 , 5.8 and $8.0\ \mu\text{m}$ still provide valuable constraints on $\xi_{\text{PAH}}^{\text{tot}}$, while the loss of *ISO* 6.75 and $15\ \mu\text{m}$ and *IRAS* $12\ \mu\text{m}$ information makes determinations of $\xi_{\text{MIR}}^{\text{tot}}$ and ξ_W^{tot} more uncertain. The lack of far-infrared information also weakens the constraints on the dust mass M_d in Fig. 10.

(ii) *Case II* (blue histograms in Figs. 10 and 11): this is similar to *Case I*, but we also relax the constraint on the *Spitzer*/*MIPS* $70\text{-}\mu\text{m}$ luminosity. The main effect is to significantly worsen estimates of the contributions to the total infrared luminosity by warm dust in thermal equilibrium (ξ_W^{tot}) and by the hot mid-infrared continuum ($\xi_{\text{MIR}}^{\text{tot}}$). The constraints on the total infrared luminosity L_d^{tot} itself are also slightly worse.

(iii) *Case III* (green histograms in Figs. 10 and 11): this is similar to *Case II*, but we also relax the constraints on the *GALEX FUV* and *NUV* luminosities. Not including information about the ultraviolet radiation from young stars has only a weak influence on the results of Figs. 10 and 11, when optical, near-infrared and mid-infrared data out to $24\ \mu\text{m}$ are already available. The constraints on the specific star formation rate (ψ_s), the attenuation parameters (μ , $\hat{\tau}_V$ and the product $\mu\hat{\tau}_V$) and the relative contribution by dust in the ambient ISM to the total infrared luminosity (f_μ) become marginally worse. The total infrared luminosity L_d^{tot} and the stellar mass M_* remain reasonably well constrained.

We note that, if a galaxy has mid-infrared colours characteristic of Galactic cirrus emission, and if no other spectral information is available at shorter and longer wavelengths to constrain f_μ , it may be difficult to disentangle the contributions by stellar birth clouds and the ambient ISM to the total infrared luminosity. Galaxies with cirrus-like mid-infrared emission in the SINGS sample tend to have low specific star formation rates and infrared spectra dominated by the emission from ambient-ISM dust (as is the case, for example, for NGC 3521 in Fig. 9a). The inclusion of either far-infrared observations to constrain the temperature of the dust in thermal equilibrium or ultraviolet and optical observations to constrain the attenuation of starlight by dust can lift the ambiguity about the origin of the infrared emission (this is illustrated by the reasonably tight constraints obtained on f_μ for NGC 3521 in all the cases considered in Fig. 10). We have checked that the predicted mid-infrared emission of the ambient ISM in these analyses is always consistent with the expectation that stellar ultraviolet photons (with $\lambda < 3500\ \text{\AA}$) are the main contributors to the excitation of PAH molecules and the stochastic heating of dust grains responsible for the hot mid-infrared continuum. This is because stars slightly older than $10^7\ \text{yr}$, which have migrated

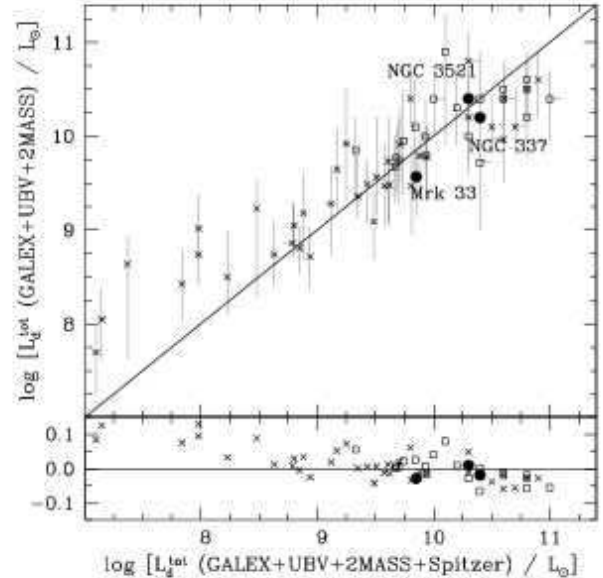


Figure 12. Estimates of the total infrared luminosity L_d^{tot} derived from fits of the observed ultraviolet (*GALEX FUV* and *NUV*), optical (RC3 *UBV*) and near-infrared (2MASS *JHKs*) luminosities, plotted against estimates of the same quantity when including also the constraints from *Spitzer* (*IRAC* 3.6 , 4.5 , 5.8 and $8.0\ \mu\text{m}$ and *MIPS* 24 , 70 , and $160\ \mu\text{m}$), for 61 galaxies with *GALEX* measurements in the sample studied in Section 3.2. The different symbols have the same meaning as in Fig. 7. The errors bars (in both the horizontal and vertical directions) represent the 16–84 percentile range in L_d^{tot} derived from the likelihood distributions. The bottom panel shows the logarithm of the difference $L_d^{\text{tot}}(\text{GALEX} + \text{UBV} + 2\text{MASS})$ minus $L_d^{\text{tot}}(\text{GALEX} + \text{UBV} + 2\text{MASS} + \text{Spitzer})$ divided by $L_d^{\text{tot}}(\text{GALEX} + \text{UBV} + 2\text{MASS} + \text{Spitzer})$.

from their birth clouds into the ambient ISM, are still bright in the ultraviolet. In the SINGS sample, for example, ultraviolet photons generated by stars older than $10^7\ \text{yr}$ account for about 5 per cent of the heating of ambient-ISM dust for galaxies with the lowest specific star formation rates (ψ_s). This fraction reaches about 85 per cent for galaxies with the highest ψ_s . At the same time, PAHs and the hot mid-infrared continuum are found to produce from about 1 per cent to about 35 per cent, respectively, of the infrared luminosity of the ambient ISM in these galaxies. Thus, enough stellar ultraviolet photons are produced to account for the mid-infrared emission from PAHs and hot dust in the ambient ISM of these galaxies, even if a large part are absorbed by cooler grains in thermal equilibrium.

The above examples illustrate the usefulness of our model to interpret multi-wavelength observations of star-forming galaxies, and how particular observations may be important to constrain specific galaxy parameters. To further investigate the need for infrared information in the determination of L_d^{tot} , we compare in Fig. 12 estimates of this quantity obtained by fitting *GALEX*, RC3 and 2MASS data alone to those obtained when adding all the *Spitzer* mid- and far-infrared constraints (from *IRAC* and *MIPS*), for 61 SINGS galaxies with *GALEX* measurements in our sample.

For most galaxies, both estimates are consistent with each other, although the estimates based on stellar emission alone are far more uncertain than those including infrared constraints (as can be seen from the much larger vertical than horizontal error bars in Fig 12). There is a tendency for starlight-based estimates of L_d^{tot} to lie systematically under the more precise estimates including infrared constraints for the most luminous galaxies. This could arise, for example, if the SINGS galaxies with the largest infrared luminosities contained significant amounts of enshrouded stars with little contribution to the emergent optical and near-infrared light. At low L_d^{tot} , starlight-based estimates of the infrared luminosities of blue compact dwarf galaxies in our sample are very uncertain in Fig 12. We conclude that rough estimates of L_d^{tot} may be obtained based on ultraviolet, optical and near-infrared observations alone (at least for values in the range from a few $\times 10^8$ to a few $\times 10^{10} L_\odot$), but reliable estimates of this parameter require longer-wavelength infrared observations. We note that the total dust luminosities estimated including infrared observations are typically within 10 per cent of those estimated by Draine et al. (2007) on the basis of their more sophisticated physical dust model.

3.2.3 Sample statistics

We can estimate the physical parameters of all the 66 SINGS galaxies in our sample in the same way as exemplified in Figs. 10 and 11 above for NGC 3521, NGC 337 and Mrk 33. By doing so, we can explore potential correlations between different parameters of star-forming galaxies and infrared colours. In Table 2, we present the results of this investigation. We list the Spearman rank correlation coefficients for the relations between three *Spitzer* infrared colours, L_ν^8/L_ν^{24} , L_ν^{24}/L_ν^{70} and L_ν^{70}/L_ν^{160} , and 11 parameters derived from our spectral fits of SINGS galaxies: the specific star formation rate, ψ_S ; the fraction of total infrared luminosity contributed by dust in the ambient ISM, f_μ ; the global contributions (i.e. including stellar birth clouds and the ambient ISM) by PAHs ($\xi_{\text{PAH}}^{\text{tot}}$), the hot mid-infrared continuum ($\xi_{\text{MIR}}^{\text{tot}}$) and warm dust in thermal equilibrium ($\xi_{\text{W}}^{\text{tot}}$) to the total infrared luminosity (equations 19, 20 and 21); the equilibrium temperature of warm dust in stellar birth clouds, T_{W}^{BC} ; the contribution by cold dust in thermal equilibrium to the total infrared luminosity, $\xi_{\text{C}}^{\text{tot}}$ (equation 22); the equilibrium temperature of cold dust in the ambient ISM, $T_{\text{C}}^{\text{ISM}}$; the star formation rate averaged over the past 100 Myr, $\psi = M_*\psi_S$ (see equation 34); the stellar mass, M_* ; and the ratio of dust mass to stellar mass, M_d/M_* (see equation 30). We also indicate in Table 2 the significance levels of these correlations for our sample size of 66 galaxies.

Table 2 shows that the infrared colours L_ν^8/L_ν^{24} and L_ν^{70}/L_ν^{160} correlate well with several model quantities, such as ψ_S , f_μ , $\xi_{\text{PAH}}^{\text{tot}}$, $\xi_{\text{W}}^{\text{tot}}$, T_{W}^{BC} , $\xi_{\text{C}}^{\text{tot}}$ and $T_{\text{C}}^{\text{ISM}}$, while L_ν^{24}/L_ν^{70} does not. Furthermore, it is interesting to note that the specific star formation rate, but *not* the star formation rate itself, correlates well with L_ν^8/L_ν^{24} and L_ν^{70}/L_ν^{160} . This is illustrated in Fig. 13, where we show L_ν^8/L_ν^{24} and L_ν^{70}/L_ν^{160} as a function of both ψ_S and ψ for the 66 galaxies in our sample. We find that, as anticipated in Section 3.2.2, the correlation between infrared colours and specific star formation rate arises from a drop in the relative intensity of PAHs and a blueshift of the peak infrared luminosity (i.e. a rise

in the overall dust temperature) when the star formation activity increases.

In Fig. 14, we explore the relations between ψ_S and other physical properties of the SINGS galaxies, which correlate well with infrared colours: f_μ , $\xi_{\text{PAH}}^{\text{tot}}$, $\xi_{\text{W}}^{\text{tot}}$, $\xi_{\text{C}}^{\text{tot}}$ and M_d/M_* (Table 2). The Spearman rank coefficients for these correlations are $r_S = -0.764$ (indicating a 6σ significance level for the sample size), -0.551 (4σ), 0.739 (6σ), -0.647 (5σ) and 0.780 (6σ), respectively. For completeness, we also show in Fig. 14 the relation between dust-to-gas mass ratio, M_d/M_H , and ψ_S , for the 35 galaxies with gas masses $M_H = M(\text{H I} + \text{H}_2)$ available from Draine et al. (2007). In this case, the Spearman rank coefficient is $r_S = -0.537$, indicating a 3σ correlation only for the reduced sample size. We note that the dust masses in Fig. 14 are typically within 50 per cent of those estimated by Draine et al. (2007) on the basis of their more sophisticated physical dust model.

The strong correlations between infrared colours and several physical quantities of the SINGS galaxies in Fig. 13 and 14 provide important insight into the link between star formation and ISM properties in galaxies. For example, we also find a 7σ correlation between the star formation rate ψ and the dust mass M_d for the 66 SINGS galaxies in our full sample, and a 5σ correlation between ψ and the gas mass M_H for the 35 galaxies with H I and H₂ measurements (not shown). To some extent, the rise in the contribution by stellar birth clouds (i.e. giant molecular clouds) to the infrared emission from a galaxy when ψ_S increases (Fig. 14a), the accompanying rise in the contribution by warm dust (Fig. 14c), the drop in that by cold dust (Fig. 14d) and the weakening of PAH features (Fig. 14b) have been anticipated in several previous studies (e.g., Helou 1986; Cesarsky et al. 1996; Silva et al. 1998; Dale et al. 2001, 2007). The originality of our approach is to *quantify* these effects by means of a simple but versatile model, which allows statistical studies of the star formation and dust properties of large samples of galaxies. It is worth emphasising that our method does not introduce these relations a priori and that they arise from our consistent treatment of stellar populations and dust in galaxies.

3.3 Comparison with previous models

The model we have developed allows one to interpret the infrared spectral energy distributions of galaxies consistently with the ultraviolet and optical emission, in terms of combined constraints on the star formation and dust properties. At the same time, the model is versatile enough that it can be used to statistically derive such properties for large samples of observed galaxies. So far, the tools most widely used to extract minimum physical quantities from infrared spectra of large samples of observed galaxies are the spectral libraries of Chary & Elbaz (2001) and Dale & Helou (2002). As an illustration, we compare here the constraints derived from our model to those that would be obtained using these libraries for the three galaxies studied in detail in Section 3.2.2 (Fig. 9).

Chary & Elbaz (2001) propose a library of template spectra to reproduce the observed correlations between the total infrared luminosity L_d^{tot} (L_{IR} in their notation) and the luminosities in individual *ISO* and *IRAS* bands, for local galaxies. This leads them to assign a unique luminosity

Table 2. Correlations between three *Spitzer* infrared colours L_ν^8/L_ν^{24} , L_ν^{24}/L_ν^{70} and L_ν^{70}/L_ν^{160} and the median likelihood estimates of several physical parameters constrained using our model, for the 66 SINGS galaxies in our sample. For each combination of infrared colour and parameter, the first row indicates the Spearman rank correlation coefficient r_S of the relation between the two quantities, while the second row indicates the significance level of the correlation for the sample size.

	ψ_S	f_μ	$\xi_{\text{PAH}}^{\text{tot}}$	$\xi_{\text{MIR}}^{\text{tot}}$	$\xi_{\text{W}}^{\text{tot}}$	T_{W}^{BC}	$\xi_{\text{C}}^{\text{tot}}$	$T_{\text{C}}^{\text{ISM}}$	ψ	M_*	M_{d}/M_*
L_ν^8/L_ν^{24}	-0.723 6σ	0.679 5σ	0.715 6σ	0.108 1σ	-0.858 7σ	-0.437 4σ	0.663 5σ	-0.318 3σ	-0.007 $< 1\sigma$	0.634 5σ	-0.377 3σ
L_ν^{24}/L_ν^{70}	0.018 $< 1\sigma$	-0.201 2σ	0.182 1σ	0.253 2σ	0.212 2σ	0.423 3σ	-0.390 3σ	-0.081 $< 1\sigma$	0.503 4σ	0.243 2σ	0.133 1σ
L_ν^{70}/L_ν^{160}	0.466 4σ	-0.464 4σ	-0.556 4σ	-0.162 1σ	0.741 6σ	0.509 4σ	0.577 5σ	0.692 6σ	-0.123 1σ	-0.450 4σ	0.040 $< 1\sigma$

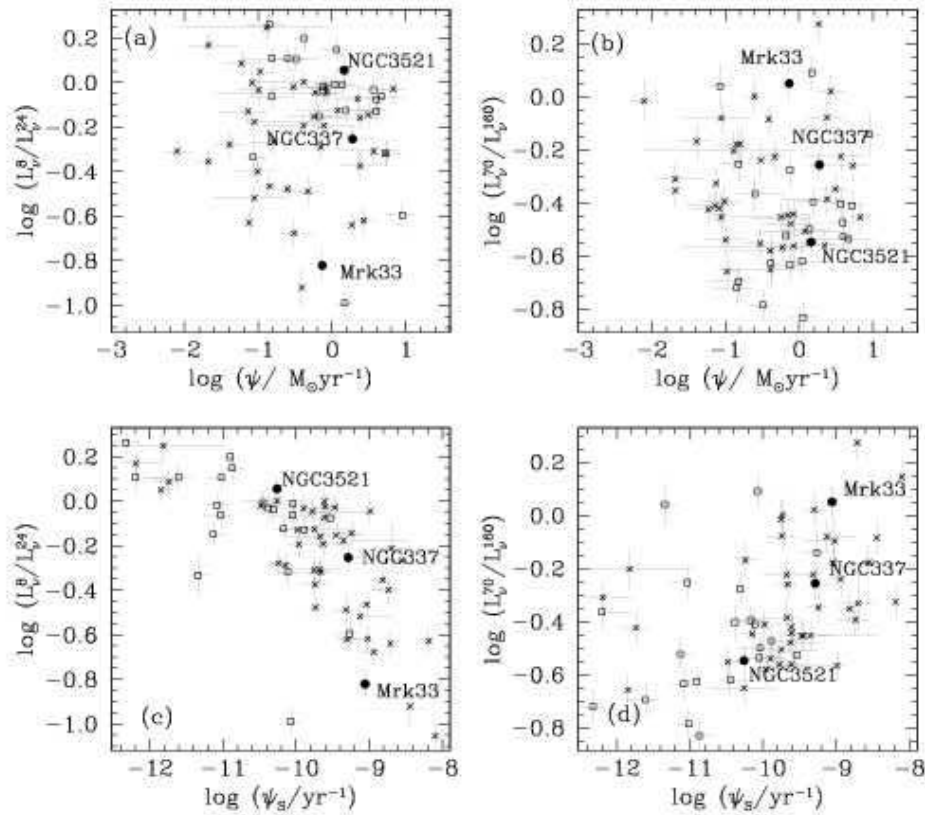


Figure 13. *Spitzer* infrared colours plotted against median-likelihood estimates of the star formation rate, for the 66 SINGS galaxies of the sample discussed in Section 3.2. (a) Ratio of 8- μm to 24- μm luminosity plotted against star formation rate averaged over the past 100 Myr, $\psi = M_*\psi_S$ (see equation 34). (b) Ratio of 70- μm to 160- μm luminosity plotted against ψ . (c) Ratio of 8- μm to 24- μm luminosity plotted against specific star formation rate ψ_S . (d) Ratio of 70- μm to 160- μm luminosity plotted against ψ_S . The different symbols have the same meaning as in Fig. 7. For each point, the vertical error bars represent the $\pm 1\sigma$ observational uncertainties, while the horizontal error bars represent the 16–84 percentile range derived from the likelihood distribution of the quantity on the x -axis.

to a given infrared spectral shape. In Fig. 15, we compare the best-fit spectral energy distributions inferred from our model for NGC 3521, NGC 337 and Mrk 33 (in black, from Fig. 9) with template spectra from Chary & Elbaz (2001, in green). Since the three galaxies have similar infrared luminosities (Fig. 11), they are assigned similar infrared spectra in the prescription of Chary & Elbaz (2001, shown as dotted green

lines in Fig. 15). However, as Figs. 7 and 9 show, NGC 3521, NGC 337 and Mrk 33 have different infrared colours. As a result, the Chary & Elbaz (2001) template spectra that best fit the *ISO* and *IRAS* colours of these galaxies (plotted as solid green lines in Fig. 15) correspond to widely different infrared luminosities. For example, the Chary & Elbaz (2001) template that best fits the observed colours of the

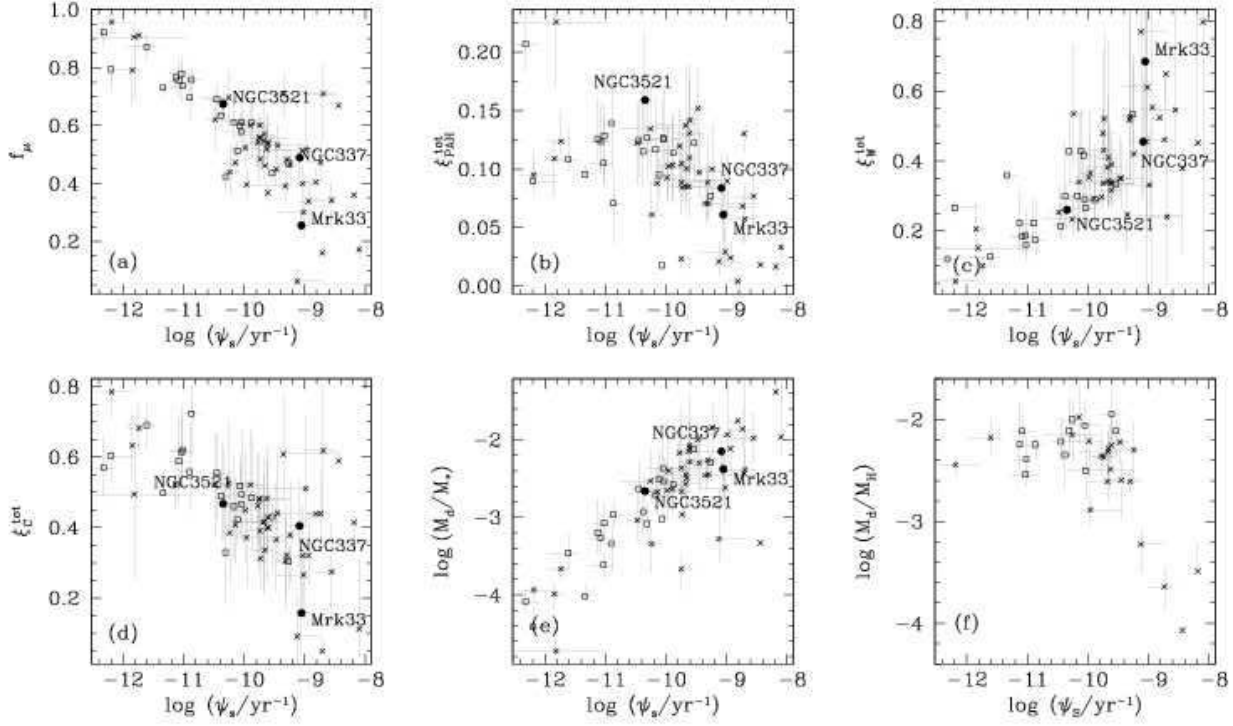


Figure 14. Median-likelihood estimates of galaxy properties plotted against specific star formation rate, for the 66 SINGS galaxies of the sample discussed in Section 3.2. (a) Fraction of total infrared luminosity contributed by dust in the ambient ISM, f_{μ} . (b) Global contribution (i.e. including stellar birth clouds and the ambient ISM) by PAHs to the total infrared luminosity, $\xi_{\text{PAH}}^{\text{tot}}$. (c) Global contribution by warm dust in thermal equilibrium to the total infrared luminosity $\xi_{\text{W}}^{\text{tot}}$. (d) Contribution by cold dust in thermal equilibrium to the total infrared luminosity, $\xi_{\text{C}}^{\text{tot}}$. (e) Ratio of dust mass to stellar mass, M_{d}/M_{\star} . (f) Ratio of dust mass to gas mass, $M_{\text{d}}/M_{\text{H}}$, for the 35 galaxies with gas masses $M_{\text{H}} = M(\text{H I} + \text{H}_2)$ available from Draine et al. (2007). The different symbols have the same meaning as in Fig. 7. The error bars represent the 16–84 percentile ranges derived from the likelihood distributions of the estimated parameters.

dwarf starburst galaxy Mrk 33 corresponds to a spectral energy distribution typical of an ultraluminous infrared galaxy (ULIRG, with $L_{\text{IR}} \geq 10^{12} L_{\odot}$). This inconsistency illustrates the impossibility with the Chary & Elbaz (2001) library to account for the intrinsic dispersion of infrared colours among galaxies of comparable infrared luminosity.

Dale & Helou (2002) parametrise the spectral energy distributions of normal star-forming galaxies in terms of a single parameter α_{SED} , which is inversely proportional to the intensity of the interstellar radiation field heating dust grains. Variations in α_{SED} can account for the observed range of F_{60}/F_{100} colours of normal star-forming galaxies. Dale et al. (2007) find that the Dale & Helou (2002) models that best fit the MIPS colours of NGC 3521, NGC 337 and Mrk 33 have $\alpha_{\text{SED}} = 3.32$, 2.23 and 1.44, respectively (these models are shown as blue lines in Fig. 15). This sequence in α_{SED} is consistent with that in the specific star formation rate ψ_{S} inferred from our analysis of these galaxies (see Fig. 10). As mentioned above, our model can provide greater insight into the star formation histories and dust properties of galaxies.

3.4 Potential sources of systematic errors

3.4.1 Star formation prior

We have checked the sensitivity of our results to the prior distributions of star formation histories in the model library of Section 3.1. We have repeated our results using continuous star formations histories (i.e. omitting superimposed stochastic starbursts). We find that, in this case, the overall quality of the fits to the ultraviolet, optical and infrared spectral energy distributions of SINGS galaxies decreases, and that the star formation rates of the galaxies are systematically lower by up to 40 per cent. We have also tested the influence of the initial mass function. Adopting a Salpeter (1955) IMF instead of the Chabrier IMF would lead to stellar mass estimates about 1.4 times larger.

3.4.2 Attenuation law

In this study, we have assumed that the effective dust absorption optical depth in stellar birth clouds scales with wavelength as $\hat{\tau}_{\lambda}^{\text{BC}} \propto \lambda^{-1.3}$ (see Section 2.1). Adopting instead $\hat{\tau}_{\lambda}^{\text{BC}} \propto \lambda^{-0.7}$ (i.e., the same wavelength dependence as the attenuation law in the ambient ISM; see Charlot & Fall 2000) does not change significantly the overall quality of the fits to the broad-band spectral energy distributions of

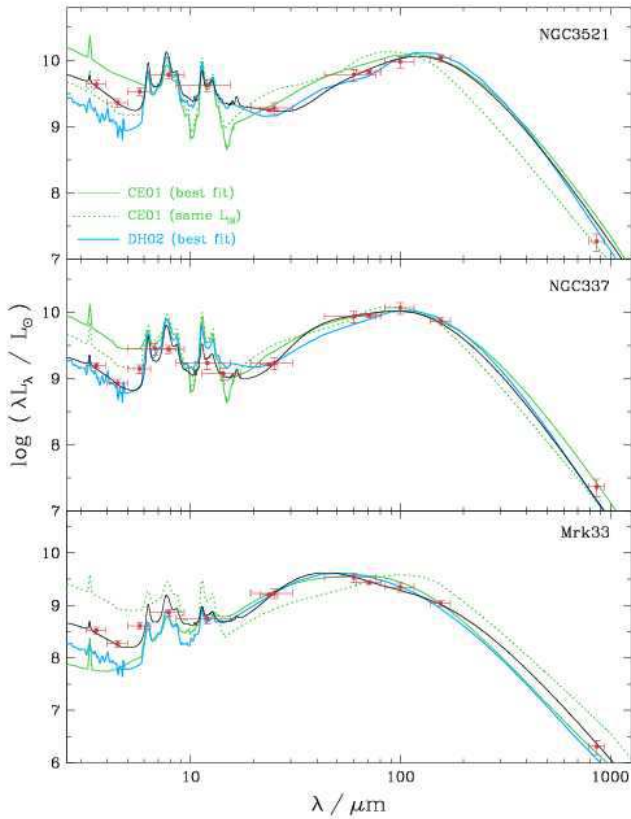


Figure 15. Fits by various models to the observed infrared (*Spitzer* IRAC and MIPS, *ISO*, *IRAS* and SCUBA) spectral energy distributions of the same three galaxies as in Fig. 9 (in red). In each panel, the black line shows the best-fit model from Fig. 9; the dotted green line is the Chary & Elbaz (2001) template spectrum corresponding to the same total infrared luminosity as the black line; the solid green line is the Chary & Elbaz (2001) template that best fits the *IRAS* and *ISO* observations of the galaxy; and the blue line is the Dale & Helou (2002) model that best fits the MIPS observations of the galaxy (see text for detail).

the SINGS galaxies. However, for the galaxies with spectroscopic observations, the $H\alpha/H\beta$ ratios predicted using $\hat{\tau}_{\lambda}^{\text{BC}} \propto \lambda^{-0.7}$ tend to be lower than observed by typically 15 per cent (see also Wild et al. 2007). This has negligible implications for the constraints on the dust parameters μ and $\hat{\tau}_V$ derived for the SINGS galaxies.

3.4.3 Inclination

The predictions of our model are averaged over viewing angles. In practice, however, because of the non-uniform spatial distribution of dust, observed fluxes at ultraviolet, optical and infrared wavelengths may depend on the angle under which a star-forming galaxy is seen. We account to some extent for this effect in our model when introducing the uncertainty δf_{μ} in the connection between stellar and dust emission (see Section 3.1). Also, we do not find any systematic trend in the quality of spectral fits with the inclination of the SINGS galaxies. In the future, we plan to investigate the effect of orientation further by applying our model to

larger samples of galaxies spanning wide ranges in physical properties and inclinations.

3.5 Applicability of the model

Our model is designed primarily to interpret ultraviolet, optical and infrared observations of large samples of (randomly oriented) galaxies in terms of effective (i.e. galaxy-wide) physical parameters, such as star formation rate, stellar mass, dust mass, total infrared luminosity, breakdown of this luminosity between different dust components and between star-forming clouds and the diffuse ISM (Section 3.2). Constraints on these quantities for statistical samples of galaxies at various redshifts are expected to provide useful insight into the processes that were important in the evolution of the galaxies we see today.

Our model is not optimised to interpret in detail multi-wavelength observations of individual galaxies, for which the consideration of geometrical factors becomes important. Studies of this type generally require complex radiative transfer calculations for specific optical properties of dust grains and specific spatial distributions of stars and dust. We refer the reader to the more sophisticated models of, for example, Silva et al. (1998) and Popescu et al. (2000) for such purposes. Also, for detailed investigations of the ambient physical conditions of gas and dust in starburst galaxies, where orientation effects are expected to be less crucial, the model of Dopita et al. (2005, see also Groves et al. 2007), which includes radiative transfer in expanding H II regions, represents a suitable alternative.

4 SUMMARY AND CONCLUSION

We have developed a simple but versatile model to interpret the mid- and far-infrared spectral energy distributions of galaxies consistently with the emission at ultraviolet, optical and near-infrared wavelengths. Our model relies on the Bruzual & Charlot (2003) population synthesis code to compute the spectral evolution of stellar populations, and on the two-component model of Charlot & Fall (2000) to compute the total infrared luminosity absorbed and reradiated by dust in stellar birth clouds and in the ambient ISM. We distribute this total infrared energy in wavelength over the range from 3 to 1000 μm by considering the contributions by four main dust components: PAH emission, mid-infrared continuum emission from hot dust, warm dust with adjustable equilibrium temperature in the range 30–60 K and cold dust with adjustable equilibrium temperature in the range 15–25 K. We keep as adjustable parameters the relative contributions by PAHs, the hot mid-infrared continuum and warm dust to the infrared luminosity of stellar birth clouds. Cold dust resides (in an adjustable amount) only in the ambient ISM, where the relative ratios of the other three components are fixed to the values reproducing the observed mid-infrared cirrus emission of the Milky Way. We find that this minimum number of components is required to account for the infrared spectral energy distributions of galaxies in wide ranges of star formation histories.

We have generated a comprehensive library of model galaxy spectra by combining a library of attenuated stellar

population spectra (built from stochastic star formation histories and dust contents) with a library of infrared emission spectra. As Fig. 9 illustrates, these models provide appropriate fits to the observed ultraviolet, optical and infrared spectral energy distributions of nearby galaxies in the SINGS sample, for which data are available from *GALEX*, RC3, 2MASS, *Spitzer*, *ISO*, *IRAS* and SCUBA (Kennicutt et al. 2003). We have used this model library to derive median-likelihood estimates of the star formation rate, stellar mass, dust attenuation, dust mass and relative contributions by different dust components to the total infrared luminosity of every SINGS galaxy in our sample. The accuracy of these estimates depends on the available spectral information. We find that, for example, although the total infrared luminosity $L_{\text{d}}^{\text{tot}}$ of a galaxy can be roughly estimated using ultraviolet, optical and near-infrared data alone (at least for values in the range from a few $\times 10^8$ to a few $\times 10^{10} L_{\odot}$), reliable estimates of this parameter require infrared observations at longer wavelengths.

A main advantage provided by our model is the capacity to study the relation between different physical parameters of observed galaxies in a quantitative and statistically meaningful way. We find that, for example, the specific star formation rate of SINGS galaxies correlates strongly not only with observed infrared colours, but also with several other properties of the galaxies, such as the fraction of total infrared luminosity contributed by dust in the ambient ISM, the contributions by PAHs, warm dust and cold dust to the total infrared luminosity and the ratio of dust mass to stellar mass. These correlations provide important insight into the link between star formation and ISM properties in galaxies. In particular, they allow one to quantify the relations between star formation rate, gas mass, dust mass, stellar mass, dust temperature and distribution of the dust between giant molecular clouds and the diffuse interstellar medium. Studies of these relations at different redshifts will have important implications for our understanding of the physical processes that dominate galaxy evolution.

Our model should be useful for interpreting data from any modern galaxy survey at ultraviolet, optical and infrared wavelengths. It can also be used to design new observations by optimizing the set of observables required to constrain specific physical parameters of galaxies. This model is meant to be used by the astronomical community and we intend to make it publicly available.

ACKNOWLEDGMENTS

We thank the anonymous referee for important suggestions, which helped improve the quality of this paper. We also thank Brent Groves, Jarle Brinchmann and Tim Heckman for comments on the manuscript, and Jakob Walcher, Armando Gil de Paz, Hervé Aussel and Hélène Roussel for helpful discussions. We are grateful to Eli Dwek for providing us with an electronic version of the *COBE*/FIRAS spectrum of the diffuse cirrus emission of the Milky Way. EdC is financed by the EU Marie Curie Research Training Network MAGPOP. This research made use of the NASA/IPAC Extragalactic Database (NED) which is operated by the Jet Propulsion Laboratory, California Institute of Technology,

under contract with the National Aeronautics and Space Administration.

REFERENCES

- Aannestad P. A., Kenyon S. J., 1979, *ApJ*, 230, 771
- Agladze N. I., Sievers A. J., Jones S. A., Burlitch J. M., Beckwith S. V. W., 1996, *ApJ*, 462, 1026
- Allamandola L. J., Hudgins D. M., Sandford S. A., 1999, *ApJ*, 511, L115
- Allamandola L. J., Tielens A. G. G. M., Barker J. R., 1985, *ApJ*, 290, L25
- Andriesse C. D., 1974, *A&A*, 37, 257
- Beichman C. A., Neugebauer G., Habing H. J., Clegg P. E., Chester T. J., eds, 1988, *Infrared astronomical satellite (IRAS) catalogs and atlases. Volume 1: Explanatory supplement Vol. 1*
- Bell E. F., 2002, *ApJ*, 577, 150
- Bevington P. R., Robinson D. K., 2003, *Data reduction and error analysis for the physical sciences. Data reduction and error analysis for the physical sciences*, 3rd ed., by Philip R. Bevington, and Keith D. Robinson. Boston, MA: McGraw-Hill, ISBN 0-07-247227-8, 2003.
- Blommaert J. A. D. L., Siebenmorgen R., Coulais A., Metcalfe L., Miville-Deschenes M.-A., Okumura K., Ott S., Pollock A., Sauvage M., Starck J.-L., 2003, *The ISO Handbook, Volume II - CAM - The ISO Camera. The ISO Handbook*, Volume II - CAM - The ISO Camera Version 2.0 (June, 2003). Series edited by T.G. Mueller, J.A.D.L. Blommaert, and P. Garcia-Lario. ESA SP-1262, ISBN No. 92-9092-968-5, ISSN No. 0379-6566. European Space Agency, 2003.
- Boselli A., Lequeux J., Sauvage M., Boulade O., Boulanger F., Cesarsky D., Dupraz C., Madden S., Viallefond F., Vigroux L., 1998, *A&A*, 335, 53
- Boulanger F., Abergel A., Bernard J.-P., Burton W. B., Desert F.-X., Hartmann D., Lagache G., Puget J.-L., 1996, *A&A*, 312, 256
- Brandl B. R., Bernard-Salas J., Spoon H. W. W., Devost D., Sloan G. C., Guilles S., Wu Y., Houck J. R., et al. 2006, *ApJ*, 653, 1129
- Brinchmann J., Charlot S., White S. D. M., Tremonti C., Kauffmann G., Heckman T., Brinkmann J., 2004, *MNRAS*, 351, 1151
- Bruzual A. G., 2007, in *IAU Symposium Vol. 241 of IAU Symposium, On TP-AGB stars and the mass of galaxies*. pp 125–132
- Bruzual G., Charlot S., 2003, *MNRAS*, 344, 1000
- Cesarsky D., Lequeux J., Abergel A., Perault M., Palazzi E., Madden S., Tran D., 1996, *A&A*, 315, L305
- Chabrier G., 2003, *PASP*, 115, 763
- Charlot S., Fall S. M., 2000, *ApJ*, 539, 718
- Chary R., Elbaz D., 2001, *ApJ*, 556, 562
- Colless M., Dalton G., Maddox S., Sutherland W., Norberg P., Cole S., Bland-Hawthorn J., Bridges T., et al. 2001, *MNRAS*, 328, 1039
- Dale D. A., Bendo G. J., et al. 2005, *ApJ*, 633, 857
- Dale D. A., Gil de Paz A., et al. 2007, *ApJ*, 655, 863
- Dale D. A., Helou G., 2002, *ApJ*, 576, 159
- Dale D. A., Helou G., Contursi A., Silberman N. A., Khatkar S., 2001, *ApJ*, 549, 215

- Dale D. A., Silberman N. A., et al. 2000, *AJ*, 120, 583
- de Vaucouleurs G., de Vaucouleurs A., Corwin Jr. H. G., Buta R. J., Paturel G., Fouque P., 1991, *Third Reference Catalogue of Bright Galaxies. Volume 1-3, XII*, 2069 pp. 7 figs.. Springer-Verlag Berlin Heidelberg New York
- Dopita M. A., Groves B. A., Fischera J., Sutherland R. S., Tuffs R. J., Popescu C. C., Kewley L. J., Reuland M., Leitherer C., 2005, *ApJ*, 619, 755
- Draine B. T., Dale D. A., et al. 2007, *ApJ*, 663, 866
- Draine B. T., Lee H. M., 1984, *ApJ*, 285, 89
- Draine B. T., Li A., 2007, *ApJ*, 657, 810
- Dunne L., Eales S., Edmunds M., Ivison R., Alexander P., Clements D. L., 2000, *MNRAS*, 315, 115
- Dunne L., Eales S. A., 2001, *MNRAS*, 327, 697
- Dwek E., Arendt R. G., Fixsen D. J., Soderoski T. J., Odegard N., Weiland J. L., Reach W. T., Hauser M. G., Kelsall T., Moseley S. H., Silverberg R. F., Shafer R. A., Ballester J., Bazell D., Isaacman R., 1997, *ApJ*, 475, 565
- Efstathiou A., Rowan-Robinson M., 1990, *MNRAS*, 245, 275
- Elbaz D., Cesarsky C. J., Chanial P., Aussel H., Franceschini A., Fadda D., Chary R. R., 2002, *A&A*, 384, 848
- Flagey N., Boulanger F., Verstraete L., Miville Deschênes M. A., Noriega Crespo A., Reach W. T., 2006, *A&A*, 453, 969
- Franceschini A., Aussel H., Cesarsky C. J., Elbaz D., Fadda D., 2001, *A&A*, 378, 1
- Gallazzi A., Charlot S., Brinchmann J., White S. D. M., Tremonti C. A., 2005, *MNRAS*, 362, 41
- Galliano F., Dwek E., Chanial P., 2007, *ArXiv e-prints*, 708
- Gil de Paz A., Boissier S., Madore B. F., Seibert M., Joe Y. H., Boselli A., Wyder T. K., Thilker D., et al. 2006, *ArXiv Astrophysics e-prints*
- Gordon K. D., Misselt K. A., Witt A. N., Clayton G. C., 2001, *ApJ*, 551, 269
- Groves B., Dopita M., Sutherland R., Kewley L., Fischera J., Leitherer C., Brandl B., van Breugel W., 2007, *ArXiv e-prints*, 712
- Helou G., 1986, *ApJ*, 311, L33
- Helou G., Lu N. Y., Werner M. W., Malhotra S., Silberman N., 2000, *ApJ*, 532, L21
- Hildebrand R. H., 1983, *QJRAS*, 24, 267
- Hoessel J. G., Saha A., Danielson G. E., 1998, *AJ*, 115, 573
- Holland W. S., Robson E. I., Gear W. K., Cunningham C. R., Lightfoot J. F., Jenness T., Ivison R. J., Stevens J. A., Ade P. A. R., Griffin M. J., Duncan W. D., Murphy J. A., Naylor D. A., 1999, *MNRAS*, 303, 659
- Hollenbach D. J., Tielens A. G. G. M., 1997, *ARA&A*, 35, 179
- Hopkins A. M., Connolly A. J., Haarsma D. B., Cram L. E., 2001, *AJ*, 122, 288
- Jarrett T. H., Chester T., Cutri R., Schneider S. E., Huchra J. P., 2003, *AJ*, 125, 525
- Kauffmann G., Charlot S., 1998, *MNRAS*, 297, L23+
- Kauffmann G., Heckman T. M., et al. 2003, *MNRAS*, 341, 33
- Kennicutt Jr. R. C., Armus L., et al. 2003, *PASP*, 115, 928
- Kessler M. F., Steinz J. A., Anderegg M. E., Clavel J., Drechsel G., Estaria P., Faelker J., Riedinger J. R., et al. 1996, *A&A*, 315, L27
- Kong X., Charlot S., Brinchmann J., Fall S. M., 2004, *MNRAS*, 349, 769
- Lagache G., Dole H., Puget J.-L., 2003, *MNRAS*, 338, 555
- Lagache G., Dole H., Puget J.-L., Pérez-González P. G., Le Floc'h E., Rieke G. H., Papovich C., Egami E., Alonso-Herrero A., Engelbracht C. W., Gordon K. D., Misselt K. A., Morrison J. E., 2004, *ApJS*, 154, 112
- Laurent O., Mirabel I. F., Charmandaris V., Gallais P., Madden S. C., Sauvage M., Vigroux L., Cesarsky C., 2000, *A&A*, 359, 887
- Lee H., Grebel E. K., Hodge P. W., 2003, *A&A*, 401, 141
- Leger A., D'Hendecourt L., Defourneau D., 1989, *A&A*, 216, 148
- Leger A., Puget J. L., 1984, *A&A*, 137, L5
- Li A., Draine B. T., 2001, *ApJ*, 554, 778
- Lu N., Helou G., Werner M. W., Dinerstein H. L., Dale D. A., Silberman N. A., Malhotra S., Beichman C. A., Jarrett T. H., 2003, *ApJ*, 588, 199
- Madden S. C., Galliano F., Jones A. P., Sauvage M., 2006, *A&A*, 446, 877
- Marcillac D., Elbaz D., Chary R. R., Dickinson M., Galliano F., Morrison G., 2006, *A&A*, 451, 57
- Marigo P., Girardi L., 2007, *A&A*, 469, 239
- Martin D. C., Fanson J., et al. 2005, *ApJ*, 619, L1
- Mathis J. S., Ruml W., Nordsieck K. H., 1977, *ApJ*, 217, 425
- Mennella V., Brucato J. R., Colangeli L., Palumbo P., Rotundi A., Bussoletti E., 1998, *ApJ*, 496, 1058
- Meurer G. R., Heckman T. M., Calzetti D., 1999, *ApJ*, 521, 64
- Misiriotis A., Popescu C. C., Tuffs R., Kylafis N. D., 2001, *A&A*, 372, 775
- Misselt K. A., Gordon K. D., Clayton G. C., Wolff M. J., 2001, *ApJ*, 551, 277
- Moustakas J., Kennicutt Jr. R. C., 2006, *ApJS*, 164, 81
- Oke J. B., Gunn J. E., 1983, *ApJ*, 266, 713
- Pope A., Scott D., Dickinson M., Chary R.-R., Morrison G., Borys C., Sajina A., Alexander D. M., Daddi E., Frayer D., MacDonald E., Stern D., 2006, *MNRAS*, 370, 1185
- Popescu C. C., Misiriotis A., Kylafis N. D., Tuffs R. J., Fischera J., 2000, *A&A*, 362, 138
- Purcell E. M., 1976, *ApJ*, 206, 685
- Rapacioli M., Joblin C., Boissel P., 2005, *A&A*, 429, 193
- Reach W. T., Dwek E., Fixsen D. J., Hewagama T., Mather J. C., Shafer R. A., Banday A. J., Bennett C. L., et al. 1995, *ApJ*, 451, 188
- Reach W. T., Megeath S. T., Cohen M., Hora J., Carey S., Surace J., Willner S. P., Barmby P., Wilson G., Glaccum W., Lowrance P., Marengo M., Fazio G. G., 2005, *PASP*, 117, 978
- Rieke G. H., Young E. T., Engelbracht C. W., Kelly D. M., Low F. J., Haller E. E., et al. 2004, *ApJS*, 154, 25
- Roussel H., Vigroux L., Bosma A., Sauvage M., Bonoli C., Gallais P., Hawarden T., Lequeux J., Madden S., Mazzei P., 2001, *A&A*, 369, 473
- Rowan-Robinson M., 1980, *ApJS*, 44, 403
- Salim S., Rich R. M., et al. 2007, *ApJS*, 704 (astro-ph/0704.3611v2)
- Salpeter E. E., 1955, *ApJ*, 121, 161
- Sellgren K., 1984, *ApJ*, 277, 623
- Sellgren K., Werner M. W., Dinerstein H. L., 1983, *ApJ*, 271, L13
- Silva L., Granato G. L., Bressan A., Danese L., 1998, *ApJ*, 509, 103

- Skrutskie M. F., Schneider S. E., Stiening R., Strom S. E., Weinberg M. D., Beichman C., Chester T., Cutri R., et al. 1997, in Garzon F., Epchtein N., Omont A., Burton B., Persi P., eds, *Astrophysics and Space Science Library* Vol. 210 of *Astrophysics and Space Science Library*, The Two Micron All Sky Survey (2MASS): Overview and Status.. pp 25–+
- Smith J. D. T., Draine B. T., et al. 2007, *ApJ*, 656, 770
- Stoughton C., Lupton R. H., Bernardi M., Blanton M. R., Burles S., Castander F. J., Connolly A. J., Eisenstein D. J., et al. 2002, *AJ*, 123, 485
- Sullivan M., Mobasher B., Chan B., Cram L., Ellis R., Treyer M., Hopkins A., 2001, *ApJ*, 558, 72
- Tuffs R. J., Popescu C. C., Völk H. J., Kylafis N. D., Dopita M. A., 2004, *A&A*, 419, 821
- Verstraete L., Pech C., Moutou C., Sellgren K., Wright C. M., Giard M., Léger A., Timmermann R., Drapatz S., 2001, *A&A*, 372, 981
- Verstraete L., Puget J. L., Falgarone E., Drapatz S., Wright C. M., Timmermann R., 1996, *A&A*, 315, L337
- Wang B., Heckman T. M., 1996, *ApJ*, 457, 645
- Werner M. W., Roellig T. L., Low F. J., Rieke G. H., Rieke M., Hoffmann W. F., Young E., Houck J. R., et al. 2004, *ApJS*, 154, 1
- Wild V., Kauffmann G., Heckman T., Charlot S., Lemson G., Brinchmann J., Reichard T., Pasquali A., 2007, *ArXiv e-prints*, 706
- Zheng X. Z., Dole H., Bell E. F., Le Floch E., Rieke G. H., Rix H.-W., Schiminovich D., 2007, *ArXiv e-prints*, 706